A new Single Sensor Based iFEM formulation for shape-sensing of thin-walled structures instrumented with single-sided sensor configurations: Formulation, numerical assessment,

Mechanical Systems and Signal Processing 232 (2025) 112700

Contents lists available at ScienceDirect

Mechanical Systems and Signal Processing

journal homepage: www.elsevier.com/locate/ymssp

A new Single Sensor Based iFEM formulation for shape-sensing of thin-walled structures instrumented with single-sided sensor configurations: Formulation, numerical assessment, and experimental validation

Vincenzo Biscotti, Marco Esposito *, Marco Gherlone

Department of Mechanical and Aerospace Engineering, Politecnico di Torino, Corso Duca degli Abruzzi 24, Torino, 10129, Italy

ARTICLE INFO

Communicated by L. Jankowski

Keywords:
Shape-sensing
iFEM
Strain sensors
Structural Health Monitoring
Displacement reconstruction
Digital twin

ABSTRACT

The reconstruction of the displacement field from discrete strain sensors, known as shape-sensing, is becoming an essential tool for realizing an efficient Structural Health Monitoring framework. In fact, monitoring displacements during service life can provide crucial information to guide preventive maintenance operations and can lead to the realization of the digital twin paradigm for the monitored structure. The shape-sensing method that has seen more success in the open literature is the inverse Finite Element Method. Although it has numerous successful applications, an obstacle to the definitive affirmation of its role as an applicable monitoring system for operating structures is the demanding requirements for numerous installed sensors. In particular, for thin-walled structures, the standard formulation of the method requires installing sensors on both faces of the structure. This configuration increases the number of sensors and is often impractical. In this work, a new Single Sensor Based inverse Finite Element (SSB-iFEM) formulation is proposed to allow the reconstruction of the deformed shape of thin-walled structures instrumented with strain sensors only on one face. The SSB-iFEM is tested numerically on a plate and on a rectangular-section box, and both numerically and experimentally on a C-section beam. The results show that extreme accuracy in monitoring can be achieved with both back-to-back and single-sided sensor configurations, thus expanding the possible applications of iFEM and opening new perspectives for its application to real operating structures.

1. Introduction

Structural components of aircraft, civil, and marine structures are prone to deterioration and require complex and costly maintenance activities. In this context, Structural Health Monitoring (SHM) techniques are rapidly evolving to provide critical information to increase safety and reduce maintenance costs [1]. Among SHM techniques, the monitoring algorithms based on displacement field reconstruction from discretely measured strains [2] have recently experienced wide success. These approaches, often referred to as *shape-sensing* methods, can compute in real-time the displacement, strain, and stress fields, which can be used for damage diagnosis or prognosis [3,4], fatigue life evaluation, or as a feedback system for the control procedure of morphing structures [5]. Moreover, the real-time capabilities of these methods make them strong candidates for the implementation of the structural *digital twin* paradigm.

* Corresponding author.
E-mail address: marco.esposito@polito.it (M. Esposito).

https://doi.org/10.1016/j.ymssp.2025.112700
Received 18 September 2024; Received in revised form 21 February 2025; Accepted 3 April 2025
Available online 18 April 2025

Several shape-sensing approaches have been developed in the open literature. They use the same inputs, the strains provided by sensors in some discrete locations, to give the same output, the displacement field, but they are based on different principles [2]. Some approaches are based on assumed spatial functions and unknown coefficients to describe the displacement field of the structure, where the coefficients are determined in order to fit the reconstructed strains to the experimental ones. In particular, the Modal Method adopts mode shapes as basis functions [6,7] that come either from a numerical model of the structure or from experimental tests. The evaluation of mode shapes often results in an onerous process, and an energy-based criterion is, therefore, necessary to select those that mainly participate in the reconstruction of the displacement field [8]. The adoption of an optimal sensor configuration can lead to accurate results even when few sensors are available [9] and recent developments include the analysis of a highly flexible wing undergoing large deformations [10]. Another important class of shape-sensing approaches is based on the integration of discretely measured strains, mainly for one-dimensional structures and using classical beam assumptions. The approach belonging to this category that has been mainly investigated is Ko's Displacement Theory. The key idea is presented in [11], i.e., the reconstruction of the deflection of a beam-like structure from double integration of axial strains measured by sensors (strain gages, optical fibers) aligned on a "sensing line" with a known distance from the neutral axis. Further to simple bending, torsional deformation can be reconstructed by either using strain gages oriented along the 45°-helical (principal) direction or by using a two-line strain-sensing system. In [12], Ko's Displacement Theory is applied to the FE model of the doubly-tapered wing of the unmanned Ikhana aircraft. In [13], an experimental assessment of Ko's shape-sensing approach is presented. Ko's Displacement Theory has also been used for the monitoring of the deformed shape of a cantilevered swept-plate wing [14] and of CFRP laminates [15]. One method that has gained increasing success in recent years is based on the Finite Element discretization of the structural domain, the inverse Finite Element Method (iFEM).

The iFEM has been introduced in [16] where, as the standard FEM, the strain field is approximated using the derivatives of known shape functions and unknown nodal degrees of freedom (DOFs). The unknown DOFs are computed by minimizing a weighted least-squares functional measuring the error between the strains due to the reconstructed displacements, discretized using finite elements, and the experimentally measured ones, in some discrete locations. The formulation is only based on the strain–displacement relations, thus it requires no information on materials or loading conditions. The iFEM was originally introduced for thin-walled structures by using the First-order Shear Deformation Theory, with the development of a three-node, triangular inverse element (iMIN3) [16], followed by quadrilateral four-node (iQS4) [17], curved eight-node [18] and iso-geometric inverse elements [19,20]. Further two-dimensional iFEM developments have been non-linear formulations for large displacements [21,22] and special formulations for multilayered composite and sandwich structures with highly heterogeneous stacking sequences [23–25]. A class of one-dimensional inverse elements based on the Timoshenko beam theory was also formulated for truss and beam structures [26] and further extended to beams with variable [27] or complex cross-sections [28]. Hybrid iFEM strategies (with a combination of one- and two-dimensional inverse finite elements) have been successfully applied to stiffened structures [29]. The inverse Finite Element Method has shown its wide applicability by finding several applications for aircraft [30–33], marine [34,35] and civil structures [36,37]. Moreover, the iFEM can be directly used to implement SHM strategies, as shown in some recent papers where iFEM-based damage-detection techniques are presented [4,38–41]. In [38,41], simple strategies are proposed to provide useful information regarding the presence, position, and orientation of damages (cracks, delaminations, debonding) in thin-walled structures. In [39], the iFEM and PeriDynamics are coupled for real-time shape-sensing analysis and crack propagation monitoring of plate structures. In [40], the focus is on internal/external defects in composites, e.g., delamination and surface debonding. A similar approach is adopted in [4], but starting from strain data coming from the harmonic and random vibrations of composite shells.

Comparative investigations available in the open literature [2,33,42,43] indicate that the Modal Method and the iFEM are the more versatile and effective shape-sensing approaches for general/complex structures. In particular, the iFEM seems to be potentially more accurate even in the presence of uncertainties but at the cost of a high number of strain input data (and corresponding strain sensors) [42,43]. For this reason, several works have been presented to tackle this limitation. An enhancement of the iFEM was presented in [44] in order to allow shape-sensing also when sparse strain data are available, in particular by including inverse shell elements without strain data by means of a penalization strategy. Moreover, some papers have investigated the optimization of sensor locations [42,45] in order to maximize the accuracy of the displacement field reconstruction for a given number of sensors. Another strategy to counterbalance the lack of a sufficient number of strain measurements is to pre-extrapolate the strain field prior to providing the input data to the iFEM [46–50]. Nevertheless, in all the formulations and applications for thin-walled structures available in the open literature, the iFEM weighted least-squares error functional is computed with respect to the membrane and bending strain measures. These quantities need strain measurements coming from sensors installed in a back-to-back configuration to be computed, thus they inherently require pairs of sensors and greatly limit the possibility of reducing their number. Moreover, the sensorization of both faces of a thin-walled structure is often impractical, if not impossible. Best to the authors' knowledge, the only strategy proposed in the open literature to deal with this issue is present in [42] where a composite wing-box is analyzed, sensors are present on the external surface only, and the assumption is made that the strain is through-the-thickness constant. It is clear that the "constant strain" assumption may lose its applicability when the plate thickness is not negligible with respect to the overall size of the structure, or in such cases (open cross-section and torsional loads) when the strain is far from being through-the-thickness constant.

The present work proposes a Single Sensor Based iFEM formulation (SSB-iFEM) to address the long-standing problem related to the application of the iFEM to real structures with a limited number of sensors. In fact, it formulates a new weighted-least-squares error functional that, instead of the *strain measures*, directly considers the *strain measurements* provided by the sensors on the structure and compares them with the analytical ones. This solution eliminates the requirement of a back-to-back sensor configuration and

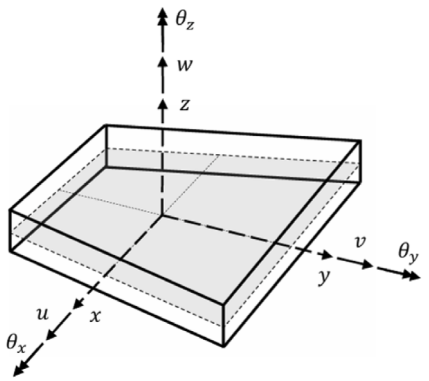

Fig. 1. Kinematic variables of FSDT [29].

offers the possibility to employ a single-sided one, reducing the number of sensors needed for the iFEM reconstruction without compromising its accuracy. The new SSB-iFEM formulation is presented and tested on three numerical examples: a thin-walled flat plate and two built-up, thin-walled structures, a rectangular section box, and a C-section beam. Additionally, to further corroborate the numerical results, an experimental campaign is conducted for the C-section beam. In these applications, the SSB-iFEM proves to be a more flexible approach than the iFEM for a wide variety of sensor configurations. In fact, it shows the same level of accuracy as the standard formulation when employing back-to-back sensor configurations. Furthermore, in the case of the built-up structures, the tests reveal that even when the sensors are deployed only on one face of the structures, the SSB-iFEM retains high accuracy, especially when compared with the iFEM, which needs back-to-back sensors to perform with comparable accuracy or experiences worse results when applied with the "constant strain" assumption.

This paper is structured as follows. In Section 2, the standard iFEM and the new SSB-iFEM formulation are illustrated, and the difference between them is highlighted. The proposed numerical and experimental test cases are described in 3 and 4, and the resulting improvements introduced by SSB-iFEM for these applications are also reported. Finally, the concluding remarks are formulated in 5.

2. Methodology

The novel 2D Single Sensor Based iFEM (SSB-iFEM) formulation introduced in this work is based on the 2D iFEM formulation first presented by Tessler et al. [16]. In this section, the original and the novel versions of the iFEM and their mathematical framework is discussed. To distinguish between the two formulations, the novel one is referred to as SSB-iFEM, whereas the original formulation is simply termed "iFEM".

2.1. iFEM formulation

The iFEM formulation is based on the minimization of a least-squares error functional over a discretized finite element domain. In the following subsection, the ingredients used for the iFEM functional are presented: the analytical and the experimental strain measures, and the expression of the iFEM functional itself.

2.1.1. Kinematic assumptions and finite element approximation

The iFEM formulation is based on the kinematic relationships of the First-order Shear Deformation Theory (FSDT) for plates or shells. According to the FSDT, the Cartesian components u_x, u_y, and u_z of the displacement vector are related to the kinematic variables $\mathbf{u} = \{u, v, w, \theta_x, \theta_y\}^T$ via the following relations:

$$\begin{aligned} u_x(x,y,z) &= u(x,y) + z\theta_y(x,y) \\ u_y(x,y,z) &= v(x,y) - z\theta_x(x,y) \\ u_z(x,y,z) &= w(x,y) \end{aligned} \tag{1}$$

where, as represented in Fig. 1, u and v are the mid-plane surface displacements, respectively in the x and y direction, w is the transverse deflection, and θ_x and θ_y are the rotations about the x and y-axes.

Combining Eq. (1) with the linear strain–displacement relations, the FSDT strain field equations are obtained:

$$\boldsymbol{\epsilon}_p = \begin{Bmatrix} \varepsilon_{xx} \\ \varepsilon_{yy} \\ \gamma_{xy} \end{Bmatrix} = \begin{Bmatrix} u_{x,x} \\ v_{y,y} \\ u_{x,y} + v_{y,x} \end{Bmatrix} = \begin{Bmatrix} u_{,x} \\ v_{,y} \\ u_{,y} + v_{,x} \end{Bmatrix} + z \begin{Bmatrix} \theta_{y,x} \\ -\theta_{x,y} \\ \theta_{y,y} - \theta_{x,x} \end{Bmatrix} = \mathbf{m}(\mathbf{u}) + z\mathbf{k}(\mathbf{u}) \tag{2}$$

$$\boldsymbol{\gamma}_s = \begin{Bmatrix} \gamma_{xz} \\ \gamma_{yz} \end{Bmatrix} = \begin{Bmatrix} u_{z,x} + u_{x,z} \\ u_{z,y} + u_{y,z} \end{Bmatrix} = \begin{Bmatrix} w_{,x} + \theta_y \\ w_{,y} - \theta_x \end{Bmatrix} = \mathbf{g}(\mathbf{u}) \tag{3}$$

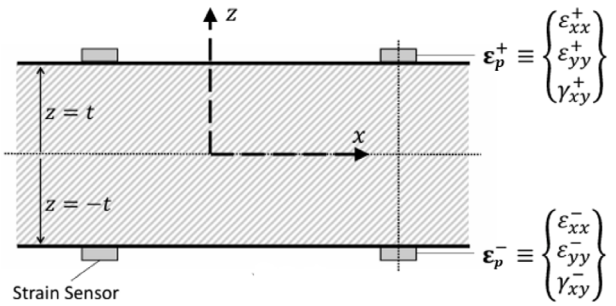

Fig. 2. Sensor instrumentation [29].

where the *in-plane strains* $\boldsymbol{\varepsilon}_p$ are expressed in terms of the in-plane *strain measures* $\mathbf{m}$ and $\mathbf{k}$, which represent respectively the in-plane stretching and bending of the reference mid-plane and, similarly, the *transverse shear strains* $\boldsymbol{\gamma}_s$ are written in terms of the *transverse shear strain measures*, $\mathbf{g}$.

As for the FEM procedure, in the iFEM the structure is subdivided into a series of finite elements, where, inside each element, the displacements are a function of the nodal degrees of freedom (DOFs) of the element and its shape functions. In particular, considering the four-node inverse finite element, the iQS4 introduced in [17] by Kefal et al. the strains within an element are approximated as:

$$\boldsymbol{\varepsilon}_p = \begin{Bmatrix} \varepsilon_{xx} \\ \varepsilon_{yy} \\ \gamma_{xy} \end{Bmatrix} = \mathbf{m}(\mathbf{u}^e) + z\mathbf{k}(\mathbf{u}^e) = \mathbf{B}^m\mathbf{u}^e + z\mathbf{B}^k\mathbf{u}^e \tag{4}$$

$$\boldsymbol{\gamma}_s = \begin{Bmatrix} \gamma_{xz} \\ \gamma_{yz} \end{Bmatrix} = \mathbf{g}(\mathbf{u}^e) = \mathbf{B}^g\mathbf{u}^e \tag{5}$$

where $\mathbf{u}^e$ is the vector containing the DOFs of the iQS4 element and $\mathbf{B}^m$, $\mathbf{B}^k$, and $\mathbf{B}^g$ are the matrices of shape functions derivatives of the inverse quadrilateral element (interested readers may refer to [17] for the expression of these terms).

2.1.2. Experimental strain measures

In the iFEM, shape-sensing is made possible by assuming that, inside the elements, a discrete number of strain sensors are present, so that the corresponding *strain measurements* are known, and the related strain measures can be computed. Considering surface-mounted strain sensors (linear strain-gauges, rosettes, or fiber-optical sensors), Fig. 2, the top-bottom experimental in-plane strain measurements, measured by back-to-back sensors placed at $z = +t$ and $z = -t$, are

$$\boldsymbol{\varepsilon}_p^+ = \begin{Bmatrix} \varepsilon_{xx}^+ \\ \varepsilon_{yy}^+ \\ \gamma_{xy}^+ \end{Bmatrix}, \qquad \boldsymbol{\varepsilon}_p^- = \begin{Bmatrix} \varepsilon_{xx}^- \\ \varepsilon_{yy}^- \\ \gamma_{xy}^- \end{Bmatrix} \tag{6}$$

respectively, and the corresponding experimental in-plane strain measures, $\mathbf{m}^\epsilon$ and $\mathbf{k}^\epsilon$, can be evaluated as:

$$\begin{aligned} \mathbf{m}^\epsilon &= \frac{1}{2}(\boldsymbol{\varepsilon}_p^+ + \boldsymbol{\varepsilon}_p^-) \\ \mathbf{k}^\epsilon &= \frac{1}{2t}(\boldsymbol{\varepsilon}_p^+ - \boldsymbol{\varepsilon}_p^-) \end{aligned} \tag{7}$$

On the other hand, since the experimental measurement of the transverse shear strains is not possible, the experimental transverse shear strain measures, $\mathbf{g}^\epsilon$, are always to be considered unavailable (in the next section, a proper explanation of how to handle this problem will be provided).

2.1.3. iFEM least-squares error functional

The definition of both the analytical strain measures of Eq. (4) and Eq. (5), and the experimental strain measures obtained with Eq. (7), allows to build, for each element of the inverse finite element discretization, the iFEM least-squares error functional:

$$\boldsymbol{\Phi}^e(\mathbf{u}^e) = \lambda_m\boldsymbol{\Phi}_m(\mathbf{u}^e) + \lambda_k\boldsymbol{\Phi}_k(\mathbf{u}^e) + \lambda_g\boldsymbol{\Phi}_g(\mathbf{u}^e) \tag{8}$$

where λ_m, λ_k, and λ_g are the vectors of penalization factors and $\boldsymbol{\Phi}_m$, $\boldsymbol{\Phi}_k$, and $\boldsymbol{\Phi}_g$ are the vectors of the individual element error functionals corresponding to the membrane, curvature and transverse shear strain measures. In particular, the explicit form of the individual error functionals of Eq. (8) is the following:

$$\boldsymbol{\Phi}_m = \begin{Bmatrix} \Phi_1 \\ \Phi_2 \\ \Phi_3 \end{Bmatrix} = \frac{1}{A^e}\int_{A^e}\left[\mathbf{m}(\mathbf{u}^e) - \mathbf{m}^\epsilon\right]^{\circ 2} dA^e = \frac{1}{A^e}\int_{A^e}\begin{Bmatrix} \left[m_1(\mathbf{u}^e) - m_1^\epsilon\right]^2 \\ \left[m_2(\mathbf{u}^e) - m_2^\epsilon\right]^2 \\ \left[m_3(\mathbf{u}^e) - m_3^\epsilon\right]^2 \end{Bmatrix} dA^e \tag{9}$$

$$\mathbf{\Phi}_k = \begin{Bmatrix} \boldsymbol{\Phi}_4 \\ \boldsymbol{\Phi}_5 \\ \boldsymbol{\Phi}_6 \end{Bmatrix} = \frac{(2t)^2}{A^e} \int_{A^e} \left[\mathbf{k}(\mathbf{u}^e) - \mathbf{k}^\epsilon\right]^{\circ 2} \, dA^e = \frac{1}{A^e} \int_{A^e} \begin{Bmatrix} \left[k_1(\mathbf{u}^e) - k_1^\epsilon\right]^2 \\ \left[k_2(\mathbf{u}^e) - k_2^\epsilon\right]^2 \\ \left[k_3(\mathbf{u}^e) - k_3^\epsilon\right]^2 \end{Bmatrix} dA^e \tag{10}$$

$$\mathbf{\Phi}_g = \begin{Bmatrix} \boldsymbol{\Phi}_7 \\ \boldsymbol{\Phi}_8 \end{Bmatrix} = \frac{1}{A^e} \int_{A^e} \left[\mathbf{g}(\mathbf{u}^e) - \mathbf{g}^\epsilon\right]^{\circ 2} \, dA^e = \frac{1}{A^e} \int_{A^e} \begin{Bmatrix} \left[g_1(\mathbf{u}^e) - g_1^\epsilon\right]^2 \\ \left[g_2(\mathbf{u}^e) - g_2^\epsilon\right]^2 \end{Bmatrix} dA^e \tag{11}$$

where A^e is the area of the element and the operator $(\cdot)^{\circ 2}$ is the Hadamard power, that is, the square power based on the Hadamard product. This operation is also known as the element-wise multiplication that, given two vectors of the same dimensions, returns a vector of the multiplied corresponding elements. The vectors of penalization factors are used to control the degree of enforcement between the analytical and measured *strain measures*, thus allowing to take into account the presence or absence of back-to-back *strain measurement* inside each element: if strain measurements are available within an element, the components of the vectors of penalization factors are set to 1 whereas, if strain measurements are unavailable, a small value, for instance 10^{-5}, is employed and a value of 0 is used for the corresponding strain measurements' components. In particular, for λ_m and λ_k, if the same component of the back-to-back in-plane strain measurement vectors, ϵ_p^+ and ϵ_p^-, is known, the corresponding component of the penalization factors is set to 1. For instance, in the case of back-to-back strain rosettes this results in $\lambda_m = \lambda_k = \{1, 1, 1\}$ as back-to-back tri-axial strains are known. On the other hand, in the case of back-to-back strain fiber measurements, where, for example, only ϵ_{xx}^+ and ϵ_{xx}^- are known, $\lambda_m = \lambda_k = \{1, 10^{-5}, 10^{-5}\}$. Lastly, in the case where in-plane strain measurements are unavailable, $\lambda_m = \lambda_k = \{10^{-5}, 10^{-5}, 10^{-5}\}$. As anticipated in the previous subsection, since transverse shear strain measures cannot be evaluated experimentally, $\mathbf{g}^\epsilon$ is always assumed to be $\mathbf{0}$, the corresponding penalization vector is always set to $\lambda_g = \{10^{-5}, 10^{-5}\}$, and the error functional related to the transverse shear measures is computed as:

$$\mathbf{\Phi}_g = \begin{Bmatrix} \boldsymbol{\Phi}_7 \\ \boldsymbol{\Phi}_8 \end{Bmatrix} = \frac{1}{A^e} \int_{A^e} \mathbf{g}(\mathbf{u}^e)^{\circ 2} \, dA^e \tag{12}$$

Substituting Eqs. (9), (10), and (12) into the definition of the element error functional provided by Eq. (8), the element error functional depends only on the element DOFs, $\mathbf{u}^e$. This means that, by minimizing the error functional with respect to the nodal DOFs, a set of linear algebraic equations is obtained

$$\frac{\partial \boldsymbol{\Phi}^e(\mathbf{u}^e)}{\partial \mathbf{u}^e} = \mathbf{K}^e\mathbf{u}^e - \mathbf{f}^e = 0 \implies \mathbf{K}^e\mathbf{u}^e = \mathbf{f}^e \tag{13}$$

where the only unknowns are the element nodal DOFs $\mathbf{u}^e$ and where the coefficient matrix $\mathbf{K}^e$ and the constant vector $\mathbf{f}^e$ are computed as:

$$\begin{aligned} \mathbf{K}^e &= \mathbf{K}_m^e + \mathbf{K}_k^e + \mathbf{K}_g^e \\ \mathbf{f}^e &= \mathbf{f}_m^e + \mathbf{f}_k^e + \mathbf{f}_g^e \end{aligned} \tag{14}$$

where

$$\begin{aligned} \mathbf{K}_m^e &= \frac{1}{A^e} \int_{A^e} \left[(\mathbf{B}^m)^T \, diag(\lambda_m) \mathbf{B}^m\right] \, dA^e \\ \mathbf{K}_k^e &= \frac{(2t)^2}{A^e} \int_{A^e} \left[(\mathbf{B}^k)^T \, diag(\lambda_k) \mathbf{B}^k\right] \, dA^e \\ \mathbf{K}_g^e &= \frac{1}{A^e} \int_{A^e} \left[(\mathbf{B}^g)^T \, diag(\lambda_g) \mathbf{B}^g\right] \, dA^e \end{aligned} \tag{15}$$

and

$$\begin{aligned} \mathbf{f}_m^e &= \frac{1}{A^e} \int_{A^e} \left[(\mathbf{B}^m)^T \, diag(\lambda_m) \mathbf{m}^\epsilon\right] \, dA^e \\ \mathbf{f}_k^e &= \frac{(2t)^2}{A^e} \int_{A^e} \left[(\mathbf{B}^k)^T \, diag(\lambda_k) \mathbf{k}^\epsilon\right] \, dA^e \\ \mathbf{f}_g^e &= \frac{1}{A^e} \int_{A^e} \left[(\mathbf{B}^g)^T \, diag(\lambda_g) \mathbf{g}^\epsilon\right] \, dA^e = \mathbf{0} \end{aligned} \tag{16}$$

Transforming from the local-element to the global-structure coordinate system, as in a typical FEM procedure, the contribution of each element matrix $\mathbf{K}^e$ and constant vector $\mathbf{f}^e$ is assembled, producing the following set of global algebraic equations

$$\mathbf{KU} = \mathbf{F} \tag{17}$$

where $\mathbf{U}$ contains the nodal displacements of the whole discretized structure. The global matrix $\mathbf{K}$ and vector $\mathbf{F}$ depend only on the sensor locations and measured strain values. Therefore, a priori knowledge about the material properties and loading conditions of the structure is not needed, and the iFEM reconstruction is possible both in static and dynamic test cases.

2.2. Single sensor based iFEM (SSB-iFEM)

As explained in Section 2.1.3, the iFEM error functional is based on the least-squares error between the analytical and the experimental strain measures. As a consequence, the computation of experimental strain measures is required in order to carry

out the iFEM analysis. However, in Section 2.1.2, in particular in Eq. (7), it was highlighted how experimental back-to-back strain measurements are always necessary to build the experimental membrane and curvature strain measures, $\mathbf{m}^{\epsilon}$ and $\mathbf{k}^{\epsilon}$. This may represent a constraint in real applications where the installation of top-bottom sensor configurations may be difficult or even impossible. Therefore, in the following section, the SSB-iFEM, a new iFEM formulation that does not require back-to-back sensor strain measurements, is presented. In order to introduce the SSB-iFEM, the kinematic model equations presented in Section 2.1.1 are first rewritten to facilitate the reader through the comprehension of its formulation and to better highlight its differences and similarities with the iFEM formulation.

2.2.1. Kinematic assumptions and finite element approximation

The SSB-iFEM is based on the same FSDT displacement field, Eq. (1), and related strain field, Eqs. (2) and (3). The in-plane strains are now rewritten in an equivalent form as:

$$\begin{Bmatrix} \varepsilon_{xx} \\ \varepsilon_{yy} \\ \gamma_{xy} \end{Bmatrix} = \begin{bmatrix} 1 & 0 & 0 & z & 0 & 0 \\ 0 & 1 & 0 & 0 & z & 0 \\ 0 & 0 & 1 & 0 & 0 & z \end{bmatrix} \begin{Bmatrix} u_{,x} \\ v_{,y} \\ u_{,y} + v_{,x} \\ \theta_{y,x} \\ -\theta_{x,y} \\ \theta_{y,y} - \theta_{x,x} \end{Bmatrix} \tag{18}$$

In compact form, Eq. (18) can be written as:

$$\boldsymbol{\varepsilon}_p(z, \mathbf{u}) = \mathbf{Z}_{\varepsilon_p}(z) \begin{Bmatrix} \mathbf{m}(\mathbf{u}) \\ \mathbf{k}(\mathbf{u}) \end{Bmatrix} \tag{19}$$

where $\mathbf{Z}_{\varepsilon_p}(z) = \begin{bmatrix} \mathbf{I} & z\mathbf{I} \end{bmatrix}$ and $\mathbf{I}$ is the 3x3 identity matrix. Introducing the iFEM discretization via the iQS4 shape functions [17] into Eq. (19), yields:

$$\boldsymbol{\varepsilon}_p(z, \mathbf{u}^e) = \mathbf{Z}_{\varepsilon_p}(z) \begin{bmatrix} \mathbf{B}^m \\ \mathbf{B}^k \end{bmatrix} \mathbf{u}^e = \mathbf{Z}_{\varepsilon_p}(z) \mathbf{B}^{mk} \mathbf{u}^e \tag{20}$$

Eq. (20) defines the analytical expression of the in-plane strains as a function of the nodal DOFs of the iQS4 elements, $\mathbf{u}^e$, through the matrix $\mathbf{B}^{mk}$ of shape function derivatives. In particular, Eq. (20) highlights the dependence of $\boldsymbol{\varepsilon}_p$ from the thickness Cartesian coordinate z via the 3×6 matrix $\mathbf{Z}_{\varepsilon_p}(z)$.

2.2.2. SSB-iFEM least-squares error functional

The SSB-iFEM least-squares error functional is defined as:

$$\Psi^e(\mathbf{u}^e) = \lambda_p^+ \Psi_p^+(\mathbf{u}^e) + \lambda_p^- \Psi_p^-(\mathbf{u}^e) + \lambda_g \Psi_g(\mathbf{u}^e) \tag{21}$$

where, as for the iFEM formulation, λ_p^+, λ_p^-, and λ_g are the vectors of penalization factors and Ψ_p^+, Ψ_p^-, and Ψ_g are the vectors of the individual element error functionals. The explicit form of the latter is presented hereafter:

$$\Psi_p^+ = \begin{Bmatrix} \Psi_1 \\ \Psi_2 \\ \Psi_3 \end{Bmatrix} = \frac{1}{A^e} \int_{A^e} \left[\boldsymbol{\varepsilon}_p\left(z^+, \mathbf{u}^e\right) - \boldsymbol{\varepsilon}_p^+ \right]^{\circ 2} dA^e \tag{22}$$

$$\Psi_p^- = \begin{Bmatrix} \Psi_4 \\ \Psi_5 \\ \Psi_6 \end{Bmatrix} = \frac{1}{A^e} \int_{A^e} \left[\boldsymbol{\varepsilon}_p\left(z^-, \mathbf{u}^e\right) - \boldsymbol{\varepsilon}_p^- \right]^{\circ 2} dA^e \tag{23}$$

$$\Psi_g = \begin{Bmatrix} \Psi_7 \\ \Psi_8 \end{Bmatrix} = \frac{1}{A^e} \int_{A^e} \boldsymbol{\gamma}_s(\mathbf{u}^e)^{\circ 2} dA^e = \frac{1}{A^e} \int_{A^e} \mathbf{g}(\mathbf{u}^e)^{\circ 2} dA^e = \boldsymbol{\Phi}_g \tag{24}$$

where $\boldsymbol{\varepsilon}_p\left(z^+, \mathbf{u}^e\right)$ and $\boldsymbol{\varepsilon}_p(z^-, \mathbf{u}^e)$ represent the analytical strains computed at the same in-plane location within the element (same (x, y) coordinates) but for two different z coordinates. For the sake of simplicity, the two z coordinates are assumed henceforth as the ones of the top and bottom surface of the element, that is, $z^+ = t$ and $z^- = -t$. Consequently, as in Section 2.1.2, $\boldsymbol{\varepsilon}_p^+$ and $\boldsymbol{\varepsilon}_p^-$ represent the back-to-back experimental strain measurements, retrieved at the same (x,y) location of the analytical strains. As observed in the previous subsection, the analytical transverse shear strains $\boldsymbol{\gamma}_s(\mathbf{u}^e)$ are identical to the transverse shear strain measures $\mathbf{g}(\mathbf{u}^e)$. Furthermore, since, as already explained in Section 2.1.2, it is not possible to measure experimentally the transverse shear strains, the expression of Eq. (24) is identical to the one of Eq. (11). Thus, the individual error functional $\boldsymbol{\Psi}_g = \boldsymbol{\Phi}_g$ represents a common term between the iFEM formulation and the SSB-iFEM formulation.

Although the expression of the SSB-iFEM element error functional in Eq. (21) is apparently very similar to the one of the iFEM error functional presented in Eq. (8), with even a common term represented by $\boldsymbol{\Psi}_g = \boldsymbol{\Phi}_g$, the explicit form of the individual error functionals of Eqs. (22) and (23) highlights the main and substantial difference between the two formulations: while in the iFEM formulation the individual error functionals are based on the *strain measures*, the individual error functionals of the SSB-iFEM formulation contain the least-squares difference between the *strain measurements*. On one hand, in the iFEM formulation, the vectors

of penalization factors λ_m and λ_k depend on whether back-to-back sensors are present, since back-to-back sensors are needed to compute the in-plane strain measures. As a consequence, it always happens that $\lambda_m = \lambda_k$, assuming either the same small component values when back-to-back strains are unavailable, or a value of 1 when back-to-back measurements are present. On the other hand, in the SSB-iFEM formulation, the vectors of penalization factors λ_p^+ and λ_p^- are used to take into account the presence of single strain measurements. Therefore, λ_p^+ and λ_p^-, can be different, as it is possible to have strain measurements only on one of the surfaces (either top or bottom) of the inverse finite element. For example, if on the top surface of an element a strain rosette is present, while on the bottom surface sensor instrumentation is missing, the two vectors of penalty factors will be set so that $\lambda_p^+ = \{1, 1, 1\}$ and $\lambda_p^- = \{10^{-5}, 10^{-5}, 10^{-5}\}$. In the case of a back-to-back configuration, $\lambda_p^+ = \lambda_p^-$ and the procedure used to assign the values to the vector of penalization factors related to the in-plane strain measurements is identical to the one previously presented in Section 2.1.3 for λ_m and λ_k. Moreover, since $\boldsymbol{\gamma}_s(\mathbf{u}^e) = \mathbf{g}(\mathbf{u}^e)$, the vector of penalization factors related to the transverse shear strains, λ_g, is identical between the iFEM and the SSB-iFEM formulation. Therefore, as previously explained in Section 2.1.3, its components are always set to small values, that is, $\lambda_g = \{10^{-5}, 10^{-5}\}$. The new definition of the individual error functionals and of the vectors of penalization factors thus represents the main difference between the iFEM formulation and the SSB-iFEM formulation: since it is not necessary to compute the strain measures, which always require back-to-back strain measurements, the SSB-iFEM error functional can be defined and minimized even when sensors are located on one face of the element and, in the same way, the vectors of penalization factors can be evaluated independently from one another, removing the necessity of a back-to-back sensor configuration on the structure.

Introducing Eq. (20) in Eqs. (22) and (23), and after setting proper values for z^+ and z^-, it becomes apparent that the SSB-iFEM element error functional of Eq. (21) depends only on the nodal DOFs of the elements. Thus, as in the iFEM, the minimization of the error functional with respect to the nodal DOFs leads to a system of linear algebraic equations:

$$\frac{\partial \Psi^e(\mathbf{u}^e)}{\partial \mathbf{u}^e} = (\mathbf{K}')^e \mathbf{u}^e - (\mathbf{f}')^e = 0 \implies (\mathbf{K}')^e \mathbf{u}^e = (\mathbf{f}')^e \tag{25}$$

where, once again, $\mathbf{u}^e$ represents the sole unknown of the problem and where the coefficient matrix and constant term are termed $(\mathbf{K}')^e$ and $(\mathbf{f}')^e$ to distinguish them from the ones obtained with the iFEM formulation. Their explicit expression is presented in the following relations:

$$\begin{aligned} (\mathbf{K}')^e &= (\mathbf{K}_p^+)^e + (\mathbf{K}_p^-)^e + \mathbf{K}_g^e \\ (\mathbf{f}')^e &= (\mathbf{f}_p^+)^e + (\mathbf{f}_p^-)^e + \mathbf{f}_g^e \end{aligned} \tag{26}$$

where

$$\begin{aligned} (\mathbf{K}_p^+)^e &= \frac{1}{A^e} \int_{A^e} \left[(\mathbf{B}^{mk})^T (\mathbf{Z}_{\varepsilon_p}(z^+))^T diag(\lambda_p^+) \mathbf{Z}_{\varepsilon_p}(z^+) \mathbf{B}^{mk} \right] dA^e \\ (\mathbf{K}_p^-)^e &= \frac{1}{A^e} \int_{A^e} \left[(\mathbf{B}^{mk})^T (\mathbf{Z}_{\varepsilon_p}(z^-))^T diag(\lambda_p^-) \mathbf{Z}_{\varepsilon_p}(z^-) \mathbf{B}^{mk} \right] dA^e \\ \mathbf{K}_g^e &= \frac{1}{A^e} \int_{A^e} \left[(\mathbf{B}^g)^T diag(\lambda_g) \mathbf{B}^g \right] dA^e \end{aligned} \tag{27}$$

and

$$\begin{aligned} (\mathbf{f}_p^+)^e &= \frac{1}{A^e} \int_{A^e} \left[(\mathbf{B}^{mk})^T (\mathbf{Z}_{\varepsilon_p}(z^+))^T diag(\lambda_p^+) \boldsymbol{\varepsilon}_p^+ \right] dA^e \\ (\mathbf{f}_p^-)^e &= \frac{1}{A^e} \int_{A^e} \left[(\mathbf{B}^{mk})^T (\mathbf{Z}_{\varepsilon_p}(z^-))^T diag(\lambda_p^-) \boldsymbol{\varepsilon}_p^- \right] dA^e \\ \mathbf{f}_g^e &= \frac{1}{A^e} \int_{A^e} \left[(\mathbf{B}^g)^T diag(\lambda_g) \mathbf{g}^\epsilon \right] dA^e = \mathbf{0} \end{aligned} \tag{28}$$

Comparing Eq. (26) with Eq. (14) it is evident that, while the terms related to the transverse shear strains are identical between the two formulations, the coefficient matrix terms related to the in-plane strains do not depend only on the derivatives of the shape functions, as in the iFEM formulation, but also on the transverse location of the sensors via the $\mathbf{Z}_{\varepsilon_p}(z^+)$ and $\mathbf{Z}_{\varepsilon_p}(z^-)$ matrices (in particular it is assumed for simplicity that $z^+ = t$ and $z^- = -t$). In the same way, also the corresponding constant terms, $(\mathbf{f}_p^+)^e$ and $(\mathbf{f}_p^-)^e$ depend on the local transverse z coordinate. Furthermore, in the SSB-iFEM, the constant terms are computed with the *strain measurements*, $\boldsymbol{\varepsilon}_p^+$ and $\boldsymbol{\varepsilon}_p^-$, instead of the *strain measures*, $\mathbf{m}^\epsilon$ and $\mathbf{k}^\epsilon$, employed in the iFEM.

As in the iFEM procedure, exploiting the FEM assembly strategy, the local contribution of each element coefficient matrix and constant term is used to construct the global coefficient matrix and the global constant term, leading to the following set of global linear algebraic equations

$$\mathbf{K}'\mathbf{U} = \mathbf{F}' \tag{29}$$

where $\mathbf{U}$ contains the nodal displacements of the whole discretized structure. The global matrix $\mathbf{K}'$ and vector $\mathbf{F}'$, like the global coefficient matrix and constant term of the iFEM, depend only on the sensor locations and measured strain values. Hence, the SSB-iFEM formulation retains the advantages of the iFEM formulation: the SSB-iFEM formulation does not require any prior knowledge of the material characteristics of the structure nor of its loading conditions. Furthermore, by computing the error between the strain measurements rather than between the strain measures, the SSB-iFEM functional can be solved even without employing back-to-back sensor configurations, removing a constraint of the iFEM formulation.

3. Numerical tests

This section contains the results of the numerical analysis run to test the SSB-iFEM formulation and to compare its performance with the original iFEM, considering flat and built-up thin-walled structures with different sensor configurations. The flat structure tested is a plate, while the built-up structures examined are a C-section beam and a rectangular section box. All of the structures are made of Aluminium 6060 ($E = 68030$ MPa, $\nu = 0.335$) and are chosen since, on one end, in the literature, the flat plate is a benchmark structure for the iFEM analysis and, on the other end, the considered built-up structures, the beam and the box, are relevant for aerospace applications, as they represent respectively a simplified model of a stringer and of a wingbox. To reconstruct the shape of these structures via the iFEM, back-to-back sensor configurations are considered, since, as explained in Section 2, back-to-back strain measurements are always compatible with both the iFEM and the SSB-iFEM analysis. As anticipated in Section 1, however, these sensor configurations are often impractical and costly: in the case of the wingbox, the interior surfaces of the thin-wall structure may be inaccessible; on the other hand, back-to-back measurements on a long stringer would require an excessive number of sensors, which may be unavailable or too expensive. As a consequence, sensor configurations with sensors placed only on one surface of the thin-walled structures are also investigated in this section. These sensor configurations are always compatible with the SSB-iFEM formulation. On the other hand, the iFEM formulation cannot be employed with these sensor configurations, unless an assumption is made on the trend of the strains through the thickness: for instance, it could be assumed that the strains are through-the-thickness constant. This assumption was employed by Esposito in [42] to successfully reconstruct the shape of a thin-walled wingbox using strain sensors only on the external surface of the structure. In this section, the results obtained using the original iFEM formulation and the assumption of constant strain along the thickness are labeled as CS iFEM (constant strain iFEM) and they are used for comparison with the SSB-iFEM results as, for the tested structures and the considered loading conditions (which will be presented in a dedicated subsection), it is reasonable to expect an almost constant trend of the strains through the thickness of the structure. Therefore, the CS hypothesis allows to employ the iFEM reconstruction even when back-to-back sensor configurations are unavailable. It is important to note that the comparison between the two formulations is not employed to demonstrate the flaws or potential of the hypothesis on which CS iFEM is based. Rather, the comparison is carried out to highlight the wider range of applications of the SSB-iFEM formulation with respect to the iFEM formulation, on which CS iFEM is based.

3.1. Notation

To simulate the structural response of the plate, the C-section beam, and the rectangular section box for a specific set of loads and constraints, a FE model is developed for all of them, resulting in a certain number of elements, N^e, and nodes, N^n (for all the structures, specific details on the FE models are provided later, in a dedicated subsection). In particular, the FE models allow to compute three structural parameters:

- the first is the matrix containing the nodal displacements of the structure, which is assumed as the reference solution when evaluating the iFEM reconstruction performance

$$\mathbf{U}_{ref} = \left[\mathbf{U}_{X,ref}, \mathbf{U}_{Y,ref}, \mathbf{U}_{Z,ref}\right] \tag{30}$$

  where $\mathbf{U}_{X,ref}$, $\mathbf{U}_{Y,ref}$, and $\mathbf{U}_{Z,ref}$ are the $N^n \times 1$ column vectors of reference displacements components along the global coordinate system (X, Y, Z), that is,

$$\mathbf{U}_{(\cdot),ref} = \{U^1_{(\cdot),ref}, \dots, U^j_{(\cdot),ref}, \dots, U^{N^n}_{(\cdot),ref}\}^T \tag{31}$$

  where the superscript j is used to refer to the generic node of the FEM discretization;
- the second parameter is represented by the matrices used as input for the iFEM analysis, which contain the top and bottom in-plane strain measurements evaluated at the centroids of the FEM elements:

$$\begin{aligned}(\boldsymbol{\varepsilon}^+_p)^e &= \left[(\boldsymbol{\varepsilon}^+_{xx})^e, (\boldsymbol{\varepsilon}^+_{yy})^e, (\boldsymbol{\gamma}^+_{xy})^e\right]\\ (\boldsymbol{\varepsilon}^-_p)^e &= \left[(\boldsymbol{\varepsilon}^-_{xx})^e, (\boldsymbol{\varepsilon}^-_{yy})^e, (\boldsymbol{\gamma}^-_{xy})^e\right]\end{aligned} \tag{32}$$

  where $(\boldsymbol{\varepsilon}^+_{xx})^e$, $(\boldsymbol{\varepsilon}^+_{yy})^e$, $(\boldsymbol{\gamma}^+_{xy})^e$ and $(\boldsymbol{\varepsilon}^-_{xx})^e$, $(\boldsymbol{\varepsilon}^-_{yy})^e$, $(\boldsymbol{\gamma}^-_{xy})^e$ are the $N^e \times 1$ column vectors containing the top and bottom in-plane centroidal strain measurements components with respect to the local (x, y, z) coordinate system of the finite elements. For each strain component, these vectors are represented with the following expression:

$$\begin{aligned}(\boldsymbol{\varepsilon}^+_{(\cdot)})^e &= \{(\varepsilon^+_{(\cdot)})^1, \dots, (\varepsilon^+_{(\cdot)})^i, \dots, (\varepsilon^+_{(\cdot)})^{N^e}\}^T\\ (\boldsymbol{\varepsilon}^-_{(\cdot)})^e &= \{(\varepsilon^-_{(\cdot)})^1, \dots, (\varepsilon^-_{(\cdot)})^i, \dots, (\varepsilon^-_{(\cdot)})^{N^e}\}^T\end{aligned} \tag{33}$$

  where the superscript i is used to represent the ith element of the FE model;
- the third is represented by the matrices of the top and bottom nodal in-plane strain measurements

$$\begin{aligned}(\boldsymbol{\varepsilon}^+_p)^n &= \left[(\boldsymbol{\varepsilon}^+_{xx})^n, (\boldsymbol{\varepsilon}^+_{yy})^n, (\boldsymbol{\gamma}^+_{xy})^n\right]\\ (\boldsymbol{\varepsilon}^-_p)^n &= \left[(\boldsymbol{\varepsilon}^-_{xx})^n, (\boldsymbol{\varepsilon}^-_{yy})^n, (\boldsymbol{\gamma}^-_{xy})^n\right]\end{aligned} \tag{34}$$

made of $N^n \times 1$ column vectors, containing the evaluation of the in-plane strain measurements components at each node of the FEM mesh, in the local (x, y, z) coordinate system, as shown below:

$$(\boldsymbol{\varepsilon}^{+}_{(\cdot)})^n = \{(\varepsilon^{+}_{(\cdot)})^1, \dots, (\varepsilon^{+}_{(\cdot)})^j, \dots, (\varepsilon^{+}_{(\cdot)})^{N^n}\}^T$$
$$(\boldsymbol{\varepsilon}^{-}_{(\cdot)})^n = \{(\varepsilon^{-}_{(\cdot)})^1, \dots, (\varepsilon^{-}_{(\cdot)})^j, \dots, (\varepsilon^{-}_{(\cdot)})^{N^n}\}^T \tag{35}$$

The matrices and vectors of Eqs. (34) and (35) allow to define the back-to-back nodal relative difference between corresponding strain measurements components as:

$$\delta\varepsilon^{j}_{(\cdot)} = \frac{|(\varepsilon^{+}_{(\cdot)})^j - (\varepsilon^{-}_{(\cdot)})^j|}{max(|(\boldsymbol{\varepsilon}^{+}_{(\cdot)})^n, (\boldsymbol{\varepsilon}^{-}_{(\cdot)})^n|)} \tag{36}$$

where, at the denominator, for each strain component, the maximum absolute value of that measured strain component, considering both top and bottom measurements, is present. Eq. (36) is employed to verify the validity of the hypothesis of constant strains along the thickness, which, as explained previously, allows to employ the original iFEM formulation even when back-to-back sensor configurations are assumed unavailable.

To assess and compare the performance of the iFEM and of the SSB-iFEM, three error parameters are considered: the first one takes into account the local reconstruction error by computing the nodal relative error between the reference and iFEM reconstructed displacement components. Considering the jth nodal reconstructed displacement along X, $U^{j}_{X,iFEM}$; Y, $U^{j}_{Y,iFEM}$; and Z directions, $U^{j}_{Z,iFEM}$, the corresponding local relative error for the generic $U^{j}_{(\cdot)}$ component is obtained using the following expression

$$err^{j}_{U_{(\cdot)}} = \frac{|U^{j}_{(\cdot),ref} - U^{j}_{(\cdot),iFEM}|}{|U^{max}_{Z,ref}|} \tag{37}$$

where $|U^{max}_{Z,ref}|$ is the maximum absolute value of the reference displacement components along the global Z-axis. As it will be shown later in detail, all the structures tested, the flat plate, the C-section beam, and the rectangular section box, are loaded in the transverse direction, which coincides with the global Z axis. Therefore, as the greatest displacements are expected in that direction, Eq. (37) allows to properly rate the relative importance of each displacement component in the evaluation of the reconstruction error, avoiding, when the reference displacements components along X or Y are very small, large and non-representative errors related to those components. A particular value of the nodal relative error is used for the second error definition, which is represented by the nodal relative error corresponding to the maximum displacement component, that is

$$err_{max(U_{(\cdot)})} = \frac{|U^{max}_{(\cdot),ref} - U^{max}_{(\cdot),iFEM}|}{|U^{max}_{Z,ref}|} \tag{38}$$

where the superscript max denotes the node where the maximum absolute value of the reference displacement component, $U^{max}_{(\cdot),ref}$, is registered. This error does not necessarily coincide with the maximum local error. However, it is considered a critical parameter as, in the case of the structures examined, high accuracy is required when reconstructing the greatest displacement in the transverse direction and, therefore, $err_{max(U_Z)}$ in particular has to be carefully monitored. The third error definition is used to measure the global displacement reconstruction error and is defined as the root mean square error (RMSE) between the reference and iFEM reconstructed displacement components

$$\mathrm{RMSE}_{U_{(\cdot)}} = \sqrt{\frac{1}{N^n}\sum_{j=1}^{N^n}(err^{j}_{U_{(\cdot)}})^2} = \sqrt{\frac{1}{N^n}\frac{\sum_{j=1}^{N^n}(U^{j}_{(\cdot),ref} - U^{j}_{(\cdot),iFEM})^2}{(U^{max}_{Z,ref})^2}} \tag{39}$$

where the weighting factor is always $1/\sqrt{N^n}$.

3.2. Plate

The flat plate is the first structure tested for the comparison between the SSB-iFEM and the iFEM formulation. The plate is 2 m long, 1 m wide, and it is assumed that its thickness is 13 mm.

3.2.1. Plate models and sensor configuration

To simulate the structural response of the structure a MSC/NASTRAN® FE model is developed. The FE model, which is presented in Fig. 3(a), is built using 200 2D CQUAD4 shell elements, resulting in a total of 231 nodes. The structure is clamped at the root cross-section and loaded at the tip in the transverse direction by two nodal forces of 100 N each. Two load cases are considered: a pure bending load case, where both forces are applied ($F1 + F2$), and a bending-torsion load case, where only the $F2$ force in Fig. 3(a) is applied. Using only 2D quadrilateral inverse finite elements, the iQS4 [17], the FE model of Fig. 3(a) is converted into the iFE model of Fig. 3(b). The same number of elements is employed for both models, so that, at the centroid of each inverse element, the tri-axial back-to-back strain measurements are known. This set of measurements is obtained, as shown in Fig. 3(b), by assuming that 400 strain rosettes are available so that all the elements of the structure are instrumented with back-to-back sensors.

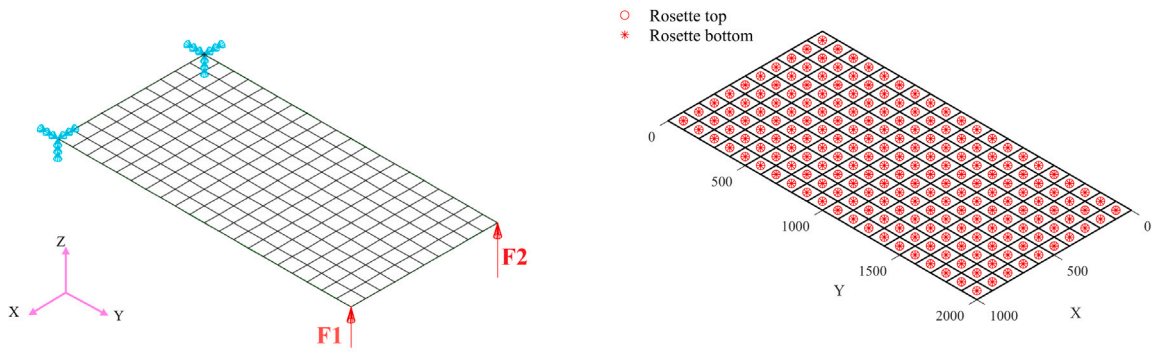

(a) FE model

(b) iFE model and sensor configuration

Fig. 3. Plate models and sensor configuration.

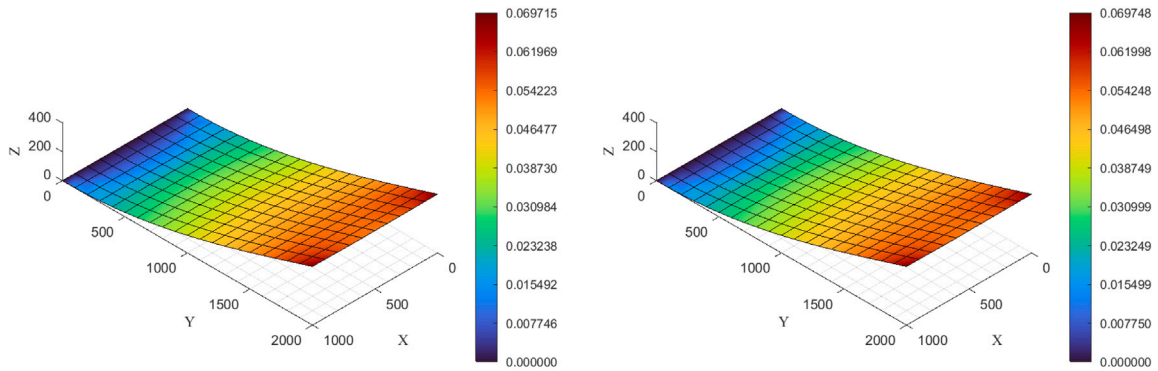

(a) iFEM

(b) SSB-iFEM

Fig. 4. Reconstructed shape colored with $err^{j}_{U_Z}$ percentage values — bending load case.

Table 1
iFEM and SSB-iFEM results - back-to-back sensors' configuration.

Formulation	iFEM	SSB-iFEM	iFEM	SSB-iFEM
Load case	Pure bending		Bending+torsion	
$RMSE_{U_Z}$ [%]	0.04048	0.04048	0.03711	0.03748
$err_{max(U_Z)}$ [%]	0.06971	0.06974	0.09460	0.09850

3.2.2. Plate results

The comparison between the iFEM and SSB-iFEM results is presented in Fig. 4 and 5, where the reconstructed deformed shape of the plate is colored with the nodal transverse displacement error, $err^{j}_{U_Z}$. The two formulations present a similar error distribution and produce almost coincident results: both the iFEM and the SSB-iFEM accurately reconstruct the shape of the structure, yielding a maximum nodal error of 0.06% for the pure bending load case and 0.09% for the bending+torsion one. These results are further corroborated by the ones of Table 1, where the comparison between the RMSE and the nodal relative error related to the maximum transverse displacement displays, again, the equivalence and the accuracy of the two reconstructions based on back-to-back sensor data.

The results presented, although promising, raise two important questions that require further discussion:

- If the two iFEM formulations seem to be equivalent when using back-to-back sensors, why do they produce non-identical results in this case?
- If the reconstruction is so accurate when using back-to-back sensors, would it be possible to use only half of the sensors, placing them only on one surface of the structure, so as to reduce the number of sensors required?

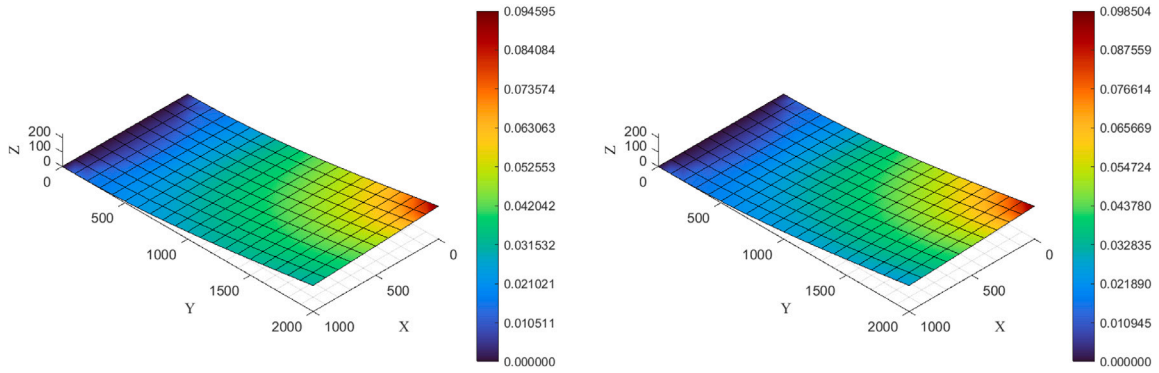

(a) iFEM (b) SSB-iFEM

Fig. 5. Reconstructed shape colored with $err^{j}_{U_z}$ percentage values — bending+torsion load case.

Table 2
Wingbox dimensions.

	Dimensions [mm]
a	960
h	460
L	3000
2t	[2,20]

To answer the first question, interested readers are invited to consult Appendix, which provides an in-depth discussion on why the two formulations do not provide identical results in the case of back-to-back sensors.

Regarding the second question, as it was explained in 2, the iFEM formulation requires back-to-back sensor configurations, thus the reconstruction would not be possible with sensors placed only on the top or the bottom surface of the elements. On the other hand, the SSB-iFEM could be employed with single-sided sensor configurations. However, in the case of a flat structure such as the plate, if the strain sensors were to be placed only on the top or only on the bottom surface of the plate, the condition number of the SSB-iFEM coefficient matrix would drastically increase, causing, as a consequence, a sharp decrease in the accuracy of the reconstruction. Nonetheless, this result is not concerning: the objective of the SSB-iFEM formulation is not to provide a method that can be employed with every sensor configuration but, rather, a new iFEM formulation that allows more flexibility when choosing the sensor configurations, as it will be proven in the following applications.

3.3. Wingbox

The second structure tested is the rectangular section box, which is used as a simplified model of a wingbox. Hence, for the rest of this section, the structure will be referred to as "wingbox".

3.3.1. Wingbox 3D model

The 3D model of the wingbox is shown in Fig. 6, and its dimensions are summarized in Table 2. Different values are considered for the thickness of the structure, $2t$, which, as shown in Table 2, ranges from 2 to 20 mm. Considering a variable thickness value allows to evaluate the performance of the SSB-iFEM and compare it with the CS iFEM: as the SSB-iFEM is independent of the assumption of constant strains along the thickness, this test aims to verify whether the SSB-iFEM formulation can improve the results of the iFEM, which, in the absence of back-to-back strain data, can only rely on some assumptions on the back-to-back strain field to substitute the missing input data.

3.3.2. Wingbox FE model

In order to simulate the structural response of the wingbox and its strain measurements, the 3D model of the wingbox presented in Fig. 6 is converted in a corresponding MSC/NASTRAN® FE model, which is shown in Fig. 7. The FE model of the wingbox is made of 324 2D CQUAD4 shell elements, which results in a total of 342 nodes. Fig. 7 also shows how the structure is clamped at one end (root cross-section) and loaded in the transverse direction at the other end with a concentrated force of 100 N. The load is applied in the shear center of the wingbox, and it is distributed with a rigid body element (RBE2) on the nodes of the tip cross-section.

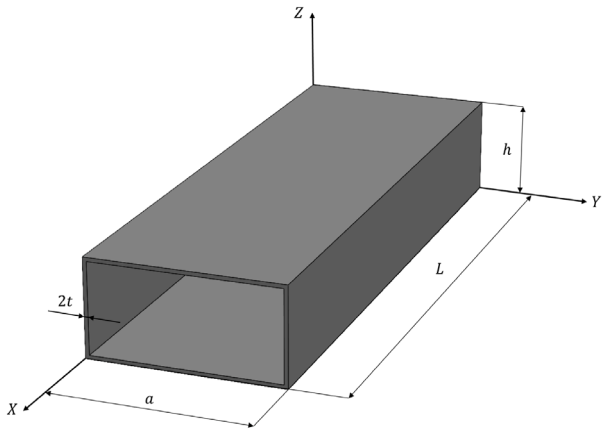

Fig. 6. Wingbox 3D model.

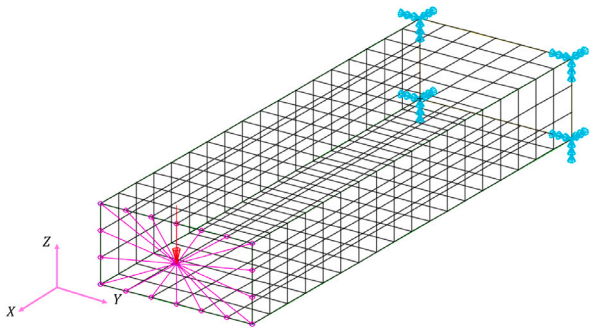

Fig. 7. Wingbox FE model.

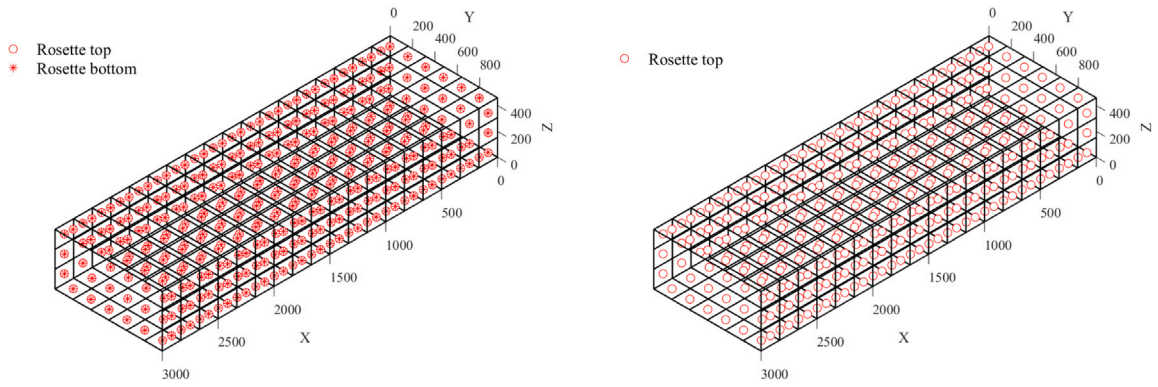

(a) Sensor configuration 1

(b) Sensor configuration 2

Fig. 8. Wingbox iFE model and sensor configurations.

3.3.3. Wingbox iFE model and sensor configurations

The iFE model of the wingbox is built using only the 2D quadrilateral inverse finite elements, the iQS4 [17], and coincides with the FE model already shown in Fig. 7. This choice guarantees full knowledge of the back-to-back strain field and provides, at the centroid of each of the inverse-finite elements, back-to-back tri-axial strain measurements. In particular, for the wingbox, two sets of input strain data are examined:

1. 648 tri-axial sensor measurements available. It is assumed that a strain rosette is mounted on the top and bottom surfaces of each inverse finite element. This sensor configuration is shown in Fig. 8(a)

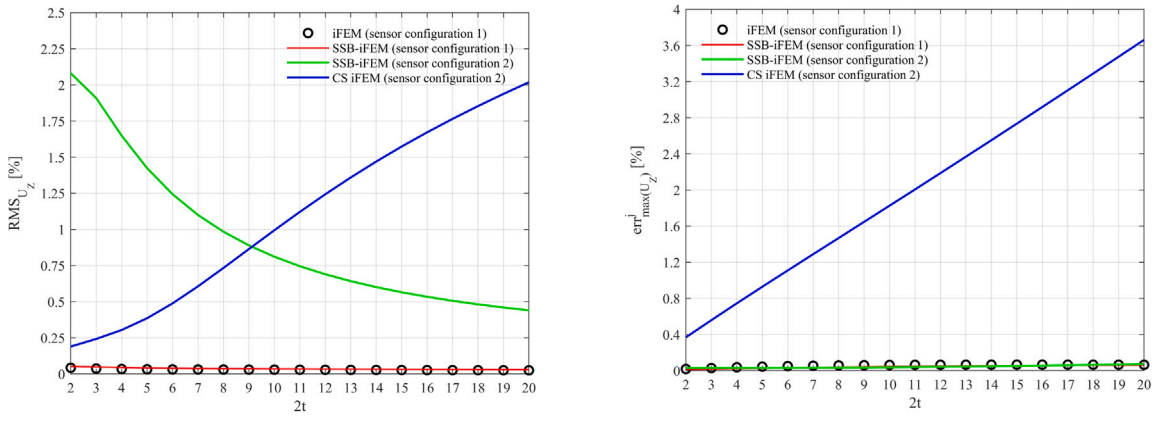

(a) RMSE$_{U_Z}$ (b) $err^j_{max(U_Z)}$

Fig. 9. iFEM analysis results for various thickness values of the wingbox.

2. 324 tri-axial strain measurements available, produced by the same number of strain rosettes, installed only on the top surface of every element, which coincides with the external surface of the wingbox. This configuration is considered particularly relevant, as in a real test case scenario it may be difficult to place sensors inside the wingbox. This second configuration is presented in Fig. 8(b)

3.3.4. Wingbox results

In Fig. 9, the results of the iFEM, the SSB-iFEM, and the CS iFEM analysis are presented, with Fig. 9(a) showing the transverse displacement root mean square error, and Fig. 9(b) the nodal relative error related to the maximum transverse displacement. Both errors are plotted against the thickness value, considering the two different sensor configurations of Fig. 8. When sensor configuration 1 is adopted, that is, when all of the tri-axial back-to-back strains are available as input data, as in the case of the flat plate, the iFEM and the SSB-iFEM produce almost coincident results (as mentioned previously, further details are presented in Appendix). On the other hand, when the measured strains are limited to those provided by sensor configuration 2, the SSB-iFEM formulation and the CS iFEM produce completely different results: considering the $err_{max(U_Z)}$, the SSB-iFEM formulation maintains an accuracy comparable to the one of the test case examined previously, yet employing half of the sensors. On the contrary, the CS iFEM results worsen considerably when the thickness rises. The same error trends can be observed when looking at the RMSE plots, with the exception of the SSB-iFEM RMSE, which, for low thickness values, is greater than the corresponding CS iFEM RMSE. The explanation of this behavior can be found by observing the results of Fig. 10, where for the cases where $2t = 2$ mm and $2t = 20$ mm, the FEM deformed shape of the wingbox is colored with the percentage values of $\delta\epsilon^j_{XX}$, the nodal difference between the strain components along the global X-axis. Comparing Fig. 10(a) with Fig. 10(b), it is evident that in both cases, at the tip of the structure ($X = 3000$ mm), $\delta\epsilon^j_{XX}$ presents a local peak: in the case of $2t = 2$ mm, this peak causes the SSB-iFEM reconstruction to produce, in the same region, a deformation of the cross-section, Fig. 11(a), that is not present in the reference solution. This erroneous reconstruction of the tip deformation is responsible for the high percentage values of the nodal transverse relative errors, $err^j_{U_Z}$, which, in turn, cause the high values of the RMSE of Fig. 9(a). On the other hand, for the structure with the higher thickness, the stiffness of the structure itself reduces the effect of the local peak of $\delta\epsilon^j_{XX}$: as shown in Fig. 11(b), the local deformation of the tip cross-section, although still present, produces smaller percentage values of the nodal relative errors when compared with the ones of Fig. 11(a). As a consequence, the RMSE value is reduced, thus resulting in the trend of Fig. 9(a). These observations confirm that the SSB-iFEM is independent of the back-to-back strain difference, as the RMSE error trend is influenced by the stiffness of the structure, rather than by $\delta\epsilon^j_{XX}$.

The colored plots of Fig. 10 also contribute to the explanation of the error trends of Fig. 9(b) associated with the SSB-iFEM and the CS iFEM analysis. As the thickness of the structure increases, the back-to-back strain difference also increases. However, as the SSB-iFEM is independent of the back-to-back strain difference, the nodal relative error related to the maximum transverse displacement of the SSB-iFEM reconstruction remains constant and very small. On the contrary, the CS iFEM continues to receive as input data the same strain values for the external and the internal surface of the wingbox, which leads to the rise of the $err^j_{max(U_Z)}$ related to the CS iFEM reconstruction.

These results highlight how the SSB-iFEM is independent of the thickness of the structure (which is directly related to the back-to-back strain difference) and, thus, they prove the wider range of applicability of the SSB-iFEM when compared to the iFEM, which, in the absence of back-to-back strain measurements, has to rely on an assumption on the through-the-thickness trend of the strain data.

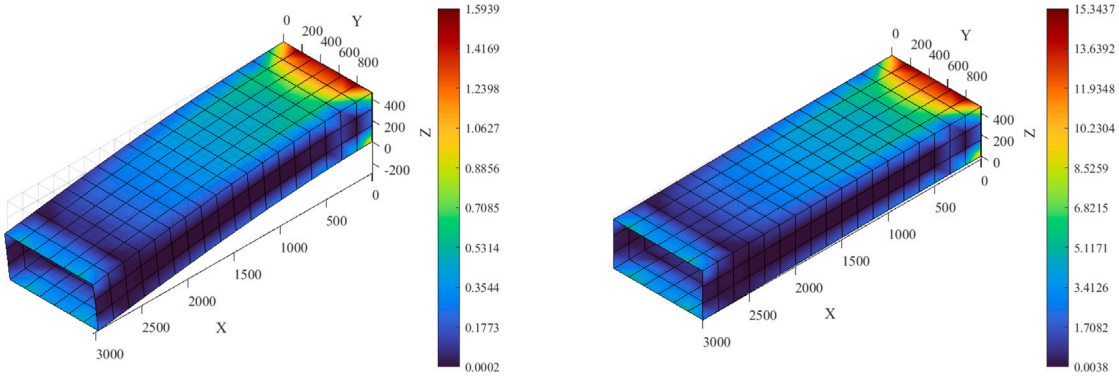

(a) $2t = 2\ mm$ (b) $2t = 20\ mm$

Fig. 10. FEM deformed shape colored with $\delta\epsilon^{j}_{XX}$ percentage values.

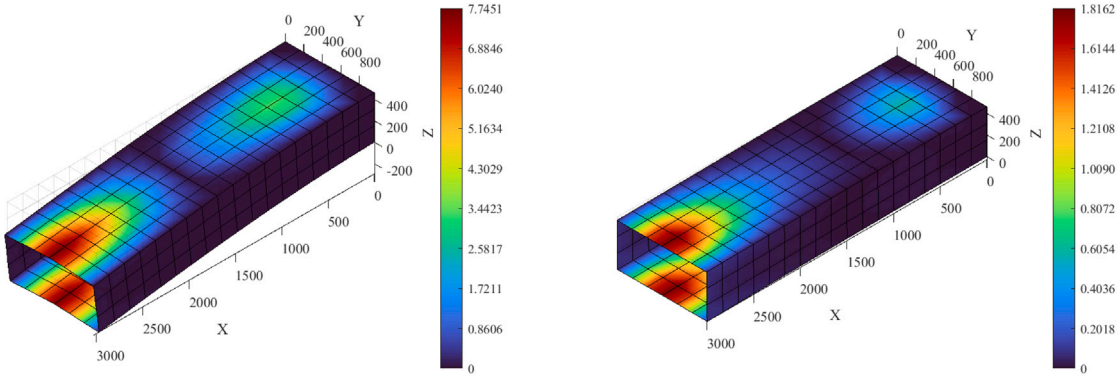

(a) $2t = 2\ mm$ (b) $2t = 20\ mm$

Fig. 11. SSB-iFEM reconstructed shape colored with $err^{j}_{U_z}$ percentage values.

Table 3
Stringer dimensions.

	Dimensions [mm]
a	30.05
h	45.2
L	1100
2t	2.08

3.4. Stringer

The last structure employed for the tests of the performance of the iFEM and of the SSB-iFEM is a C-section beam, which represents a simplified model of a stiffening structure, like a stringer, present in aircraft wings. Hence, as for the rectangular section box, the C-section beam will be referred to hereafter as "stringer"

3.4.1. Stringer 3D model

In Fig. 12, the 3D model of the stringer is presented, and Table 3 contains the dimensions of the structure. Differently from the wingbox case study, the thickness of the structure is considered fixed. The reason is that, since open cross-section structures can produce a greater variation throughout the thickness of the strain field, the focus of the numerical comparison is shifted toward the possible sensor configurations employed to retrieve the strain field.

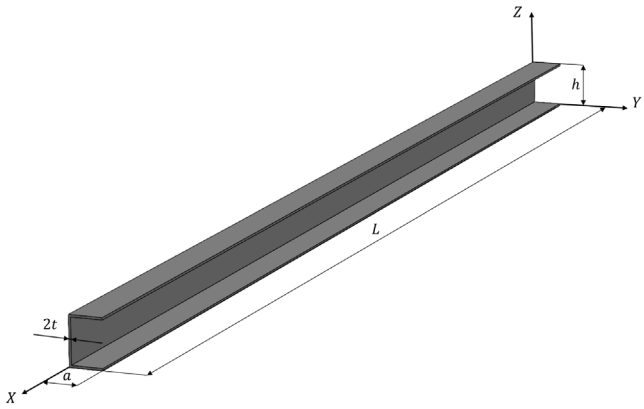

Fig. 12. Stringer 3D model.

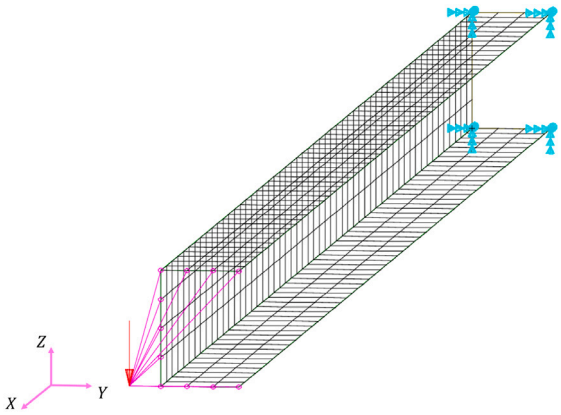

Fig. 13. Stringer FE model.

3.4.2. Stringer FE model

A MSC/NASTRAN® FE model is used to produce the reference displacements and simulate the input strain measurement. The FE model is presented in Fig. 13: it is made of 616 nodes and 550 CQUAD4 elements. The stringer is considered a cantilevered structure, clamped at its root and loaded at the tip with a transverse force of 39.24 N. As for the wingbox, the load is distributed to the nodes of the tip cross-section through a RBE2, and it is located at a distance of 11.6 mm from the middle line of the web of the stringer (the vertical segment of the section), so that it is aligned with the shear center of the section and, thus, the structure is subject to bending only.

3.4.3. Stringer iFE model and sensor configurations

The iFE model of the stringer coincides with its FE model: the structure is discretized with 550 iQS4 [17] elements, so that, at every element centroid, the tri-axial back-to-back in-plane strain measurements are known. The complete set of these measurements, however, is not always provided as input for the iFEM analysis. To test the effect of different sets of strain data on the iFEM, SSB-iFEM, and CS iFEM, four different sensor configurations (Fig. 14) are defined, corresponding to four different amounts of input strain measurements:

1. 1100 tri-axial strain measurements, corresponding to a sensor configuration where every inverse element is equipped with a strain rosette on its top and bottom surface (Fig. 14(a));
2. 1100 mono-axial strain measurements along the global X-axis. It is assumed that this set of strain data is provided by a back-to-back configuration of 20 optical fibers, placed on each row of inverse finite elements along the global X-axis (Fig. 14(b));
3. 550 mono-axial strain measurements along the global X-axis, obtained by considering only the strain measurements on the top surface of the inverse elements, that is, assuming that only half of the optical fibers of configuration 2 are available (Fig. 14(c)). The top surface of each element coincides with the external surface of the structure, which is the one closest to the load of Fig. 13;

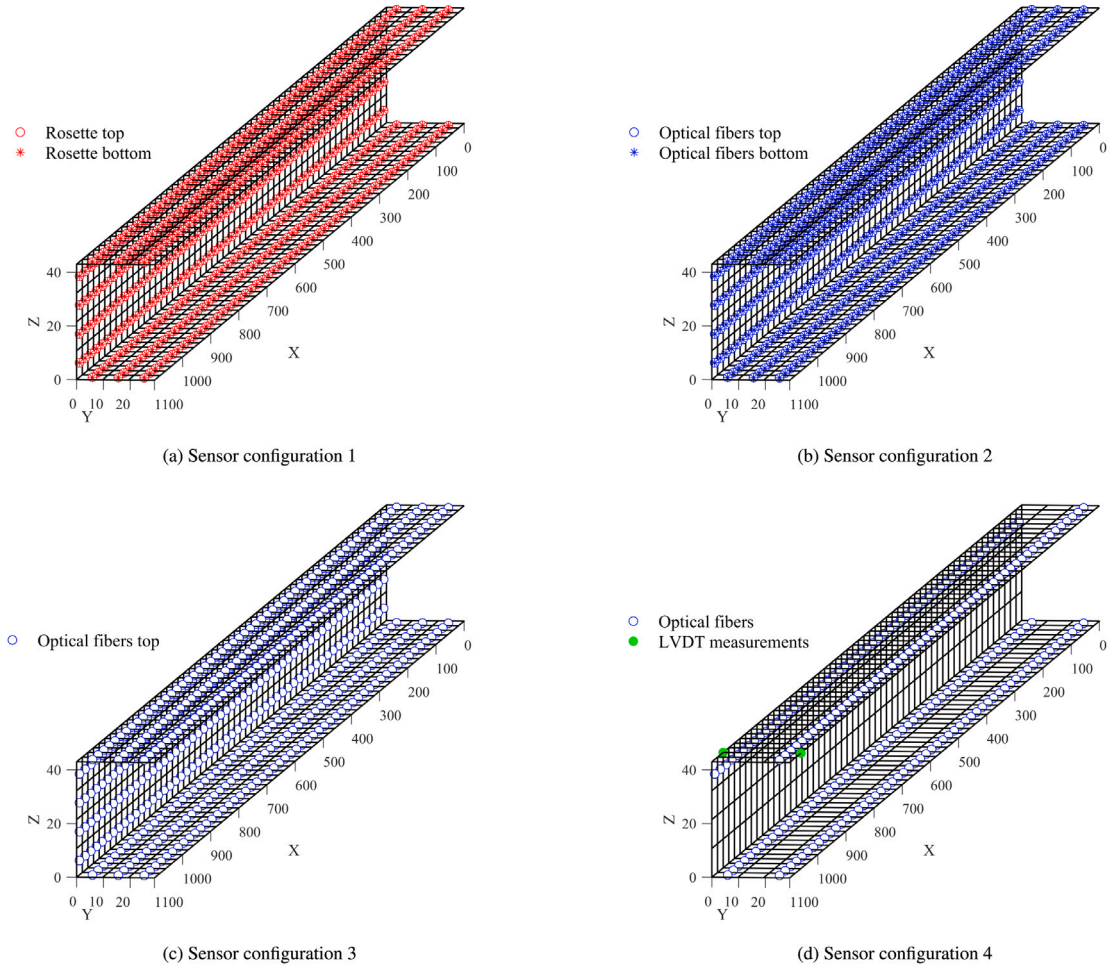

(a) Sensor configuration 1

(b) Sensor configuration 2

(c) Sensor configuration 3

(d) Sensor configuration 4

Fig. 14. Stringer iFE model, sensor configurations, and LVDT's location.

4. 220 mono-axial strain measurements along the global X-axis, corresponding to the set of strain data extracted by four optical fibers placed on the external surface of the structure (Fig. 14(d)).

3.4.4. Stringer results

For the first two sensor configurations, the SSB-iFEM reconstructed deformed shapes, colored with the nodal transverse displacement errors, are represented in Figs. 15(a) and 15(b). Furthermore, the results, in terms of the RMSE and the nodal relative error related to the maximum displacements are summarized in Table 4. Both the colored plots and the results presented in the table highlight that the iFEM and the SSB-iFEM produce extremely accurate results (the errors are always lower than 1%). Moreover, the conclusions already reached in the plate and in the wingbox case studies are further reinforced: when employing back-to-back sensor configurations, the two formulations, the iFEM and the SSB-iFEM, are perfectly equivalent. However, as in the previous test cases, it is also apparent that they are not identical (refer again to Appendix for further details).

For the third sensor configuration, as only the strain measurements on the external surface of the structure are available, the comparison between the SSB-iFEM formulation and the CS iFEM is considered. Comparing the reconstructed deformation plots of Fig. 16, it can be noticed that, in the one related to the CS iFEM (Fig. 16(a)), the reconstructed shape of the stringer presents a torsion that is clearly unacceptable since the structure is loaded in the shear center. The entity of the errors of the CS iFEM reconstruction is highlighted by the plot colors, which show how the percentage value of the nodal transverse displacement error, $err^{j}_{U_Z}$, reaches a peak of over 40%. On the other hand, the reconstructed shape obtained by the SSB-iFEM formulation, shown in Fig. 16(b), coherently with the results obtained with the first two sensor configurations, shows a structure subjected to bending only, and produces local errors with a peak that caps at less than 0.6%.

The results of Fig. 16 are corroborated by the ones of Table 5. In the transverse direction, both the RMSE and the nodal relative error for the maximum displacements are greater than 10% for the CS iFEM. In comparison, the SSB-iFEM formulation continues to

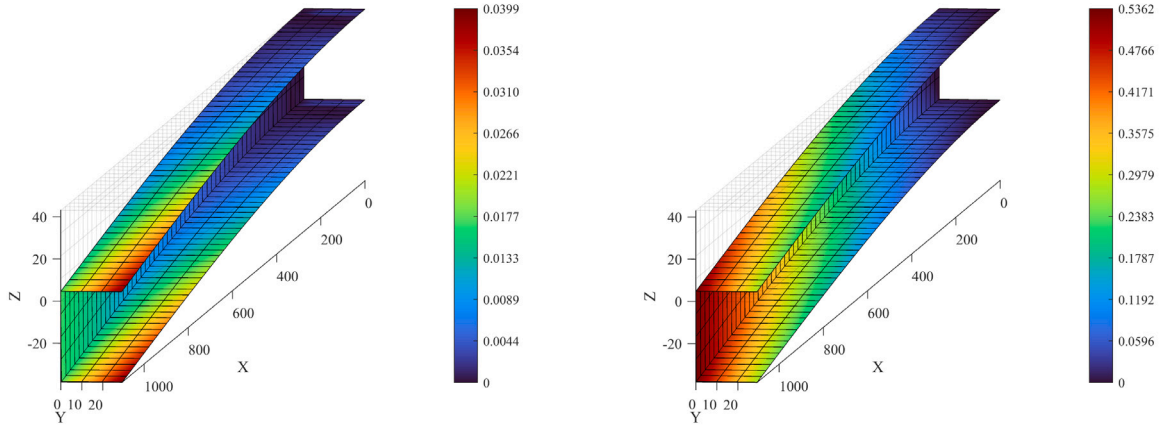

(a) Sensor configuration 1 (b) Sensor configuration 2

Fig. 15. SSB-iFEM reconstructed shape colored with $err^{i}_{U_Z}$ percentage values.

Table 4
iFEM and SSB-iFEM results — sensor configuration 1 and 2.

Formulation	iFEM	SSB-iFEM	iFEM	SSB-iFEM
Sensor configuration	1		2	
$RMSE_{U_X}$ [%]	0.0002	0.0002	0.0006	0.0007
$RMSE_{U_Y}$ [%]	0.0061	0.0074	0.1126	0.1023
$RMSE_{U_Z}$ [%]	0.0118	0.0135	0.2116	0.2526
$err_{max(U_X)}$ [%]	0.0003	0.0003	0.0001	0.0002
$err_{max(U_Y)}$ [%]	0.0139	0.0169	0.0232	0.0447
$err_{max(U_Z)}$ [%]	0.0157	0.0173	0.4746	0.5362

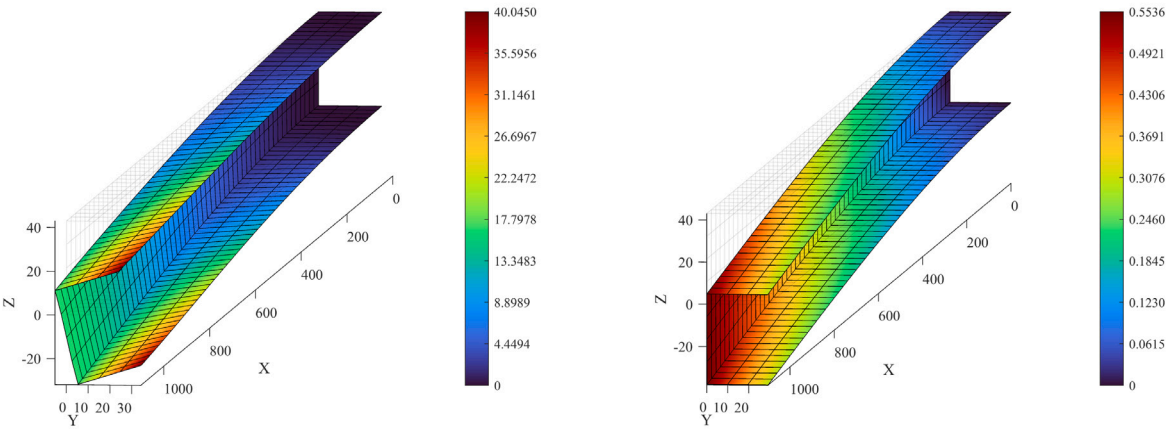

(a) CS iFEM (b) SSB-iFEM

Fig. 16. Reconstructed shape colored with $err^{i}_{U_Z}$ percentage values — sensor configuration 3.

achieve error values lower than 1%, despite employing half of the sensors of configuration 2. Moreover, as the CS iFEM produces an unrealistic torsion, the error values related to the displacement component along the Y-axis rise considerably while they remain almost constant for the SSB-iFEM. These results contribute to highlight the independence of the SSB-iFEM formulation from the back-to-back sensor measurements, thus showing its greater flexibility when compared with the iFEM formulation, which requires an assumption on the strain field (in this case scenario, the CS assumption) in the absence of back-to-back strain data.

Even when reducing the number of sensors to the ones of configuration 4, similar results to the ones presented beforehand can be observed: as shown in Fig. 17(a), the CS iFEM reconstructs, again, an unrealistic torsion, producing a maximum nodal transverse

Table 5
CS iFEM and SSB-iFEM results — sensor configuration 3.

Formulation	CS iFEM	SSB-iFEM
Sensor configuration	3	
$RMSE_{U_X}$ [%]	0.0985	0.0006
$RMSE_{U_Y}$ [%]	6.016	0.0933
$RMSE_{U_Z}$ [%]	13.11	0.2749
$err_{max(U_X)}$ [%]	0.2210	0.0003
$err_{max(U_Y)}$ [%]	13.20	0.0562
$err_{max(U_Z)}$ [%]	16.93	0.5536

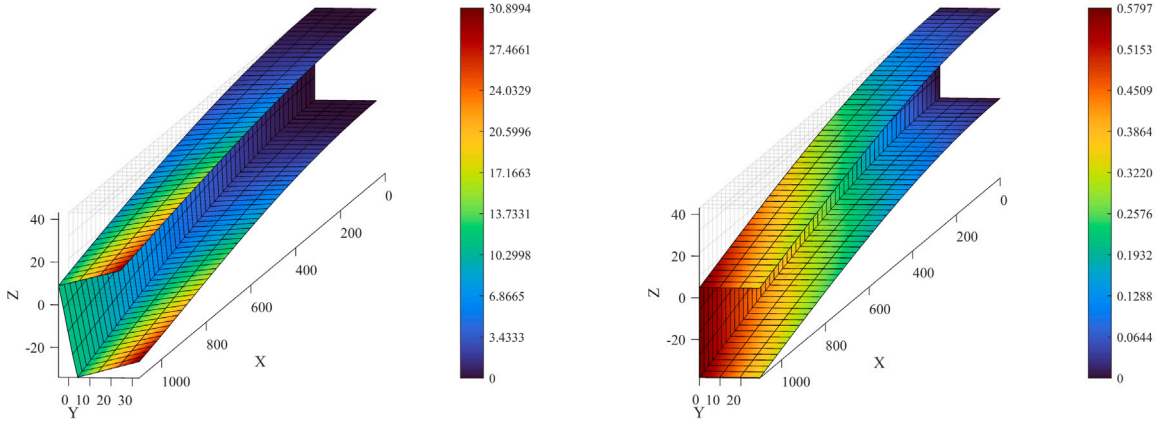

(a) CS iFEM (b) SSB-iFEM

Fig. 17. Reconstructed shape colored with $err^j_{U_Z}$ percentage values — sensor configuration 4.

Table 6
CS iFEM and SSB-iFEM results — sensor configuration 4.

Formulation	CS iFEM	SSB-iFEM
Sensor configuration	4	
$RMSE_{U_X}$ [%]	0.0875	0.0008
$RMSE_{U_Y}$ [%]	5.161	0.0866
$RMSE_{U_Z}$ [%]	9.67	0.2909
$err_{max(U_X)}$ [%]	0.2042	0.0002
$err_{max(U_Y)}$ [%]	12.02	0.0804
$err_{max(U_Z)}$ [%]	11.30	0.5797

displacement error of 30%. On the contrary, the SSB-iFEM proves to be extremely accurate even with this sensor configuration: as reported in Table 6, both the RMSE and nodal relative error values do not exceed the 1% threshold.

These results prove again the capability of the SSB-iFEM formulation to deal with multiple sensor configurations, even with those employing fewer sensors: since no assumption is made on the back-to-back strain measurements, as, unlike the iFEM formulation, they are not required as input for the analysis, the SSB-iFEM is capable of accurately reconstructing the shape of the stringer using just the sensors of configuration 4.

This observation is further corroborated by the colored plots of Fig. 18, where the nodal strain difference $\delta\varepsilon^j_{XX}$ is used to color the FEM deformations. As shown in the figure, the maximum top-bottom strain difference is greater than 10% and almost comparable to the one registered in Fig. 10(b) for the 20 mm thick wingbox, even though the stringer is just 2 mm thick. As a consequence, even for low thickness values, the assumption of constant strains along the thickness can lead to a poor iFEM reconstruction. Instead, as SSB-iFEM ignores this strain difference, its accuracy remains high, producing, in turn, accurate shape reconstructions.

4. Experimental test

This section contains the results of the experimental test conducted to corroborate the results of the previous numerical analysis. In particular, the experimental test focuses on a sensor configuration where no back-to-back strain measurement is present, to show the flexibility of the SSB-iFEM and its efficacy in reconstructing the displacement field even when employing a single-sided sensor

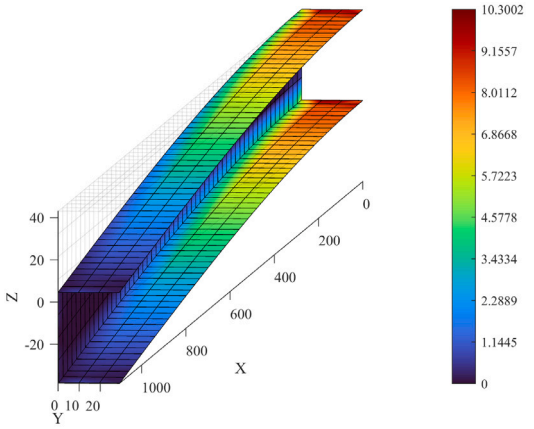

Fig. 18. FEM deformed shape colored with $\delta\epsilon^{j}_{XX}$ percentage values.

Table 7
Experimental results.

	LVDT-1			LVDT-2		
	Experimental	CS iFEM	SSB-iFEM	Experimental	CS iFEM	SSB-iFEM
U_Z [mm]	−3.42	−3.09	−3.46	−3.35	−2.35	−3.32
err_{U_Z} [%]		9.5	1.3		30	1.0

configuration. The experimental activity has been conducted at the "LAQ-AERMEC Aeromechanical Structural Systems" laboratory of the Department of Mechanical and Aerospace Engineering at Politecnico di Torino.

4.1. Experimental setup

The tested specimen is the C-section beam introduced in Section 3.4 and presented in Fig. 12. This structure is considered because, as mentioned previously, it represents a typical aerospace stiffening structure. The dimensions of the C-section beam are reported in Table 3, and the material is the Aluminium 6060, as in the numerical example ($E = 68030$ MPa, $\nu = 0.335$). The loading and boundary conditions are also the same as the ones presented in the numerical example: the beam is tested as a cantilever, by clamping the root section, and it is loaded at the tip by a concentrated transverse force, F, of 39.4 N. The load at the tip is applied through an assembly made of two beams, and the position of the load is adjusted so that it is applied in the shear center of the C-section beam. Thus the pure bending loading condition of the numerical tests is reproduced. Furthermore, a wooden central core is placed at the tip section, to avoid its deformations and to replicate the RBE2 boundary conditions. This loading assembly, as well as the clamping one, are shown in Fig. 19. Furthermore, a detailed image of the tip loading assembly is presented in Fig. 20(a), where the displacement measuring system is also visible: it consists of two LVDTs, which are placed at 4 cm from the tip of the beam. The LVDTs' measurements are used to verify the accuracy of the iFEM reconstruction and, therefore, are placed in correspondence with the iFEM mesh nodes not covered by the loading assembly and closest to the tip of the structure. The iFEM mesh is the same as the one employed in the numerical analysis. Together with the LVDTs' location, it is presented in Fig. 14(d), which, additionally, shows the experimental sensor configuration, consisting of 4 optical fibers. The fiber optic sensors are instrumented on the beam as shown in Fig. 20(b). Through the Rayleigh backscatter principle [51], they provide highly dense strain measurements in the direction of the longitudinal axis of the beam. In particular, as the strain measurements are spaced from one to the other by a gauge pitch of 1.3 mm, every inverse element along the sensing line is provided with the corresponding strain measurement.

4.2. Experimental results

In Table 7, the results of the experimental test are presented in terms of transverse displacement values, U_Z, and nodal relative error, err_{U_Z}. The SSB-iFEM results are compared to those obtained through the LVDTs' measurements and the original iFEM reconstruction. As in the previous Section, to employ the original iFEM in the absence of back-to-back measurements, the hypothesis of through-the-thickness constant strains (CS) is adopted, thus the results are termed CS iFEM.

The experimental results of Table 7 show that, for both of the LVDTs, the CS iFEM is not able to reconstruct the deformed shape of the structure. On the other hand, the low SSB-iFEM errors highlight the accuracy of the new formulation. Thus, these experimental results confirm the conclusions of the numerical analysis: the SSB-iFEM formulation provides greater flexibility than the original iFEM when choosing the sensor configuration and allows, in the case of built-up structures such as the C-section beam, to reduce the number of sensors necessary for highly accurate reconstructions.

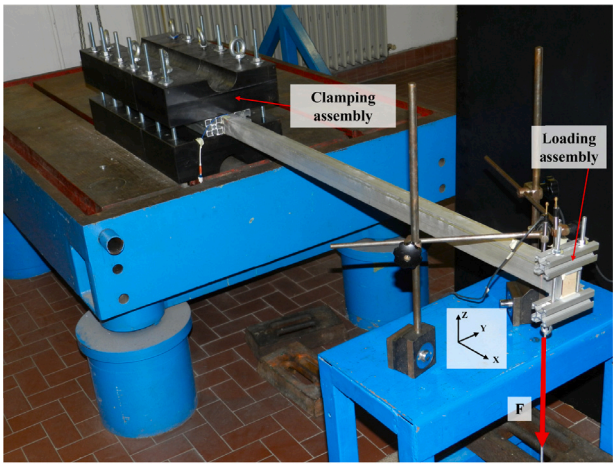

Fig. 19. Clamping and loading assembly.

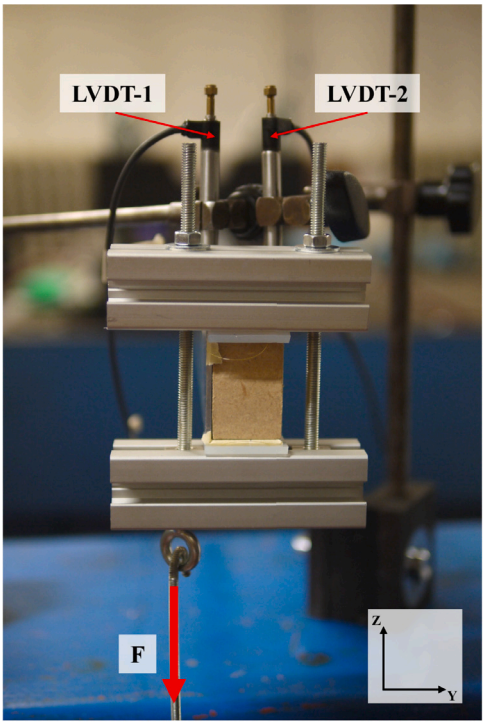

(a) Loading assembly and displacements measuring system

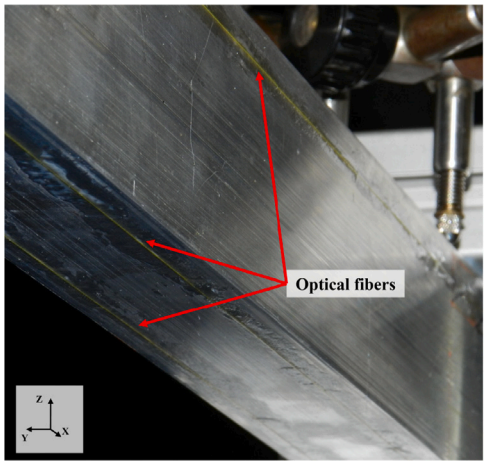

(b) Optical fibers instrumented on the beam

Fig. 20. Experimental setup details.

5. Conclusions

This work introduces a new Single Sensor Based inverse Finite Element Method (SSB-iFEM) to solve the requirement of back-to-back sensors for the displacement reconstruction of thin-walled structures. In fact, the standard iFEM formulation is based on minimizing the error between measured and analytical strains, computed in terms of membrane and bending strain measures. These quantities require sensors on both faces of a thin-walled structure to be computed. On the contrary, the novel formulation introduces a new error functional, directly expressing the error between the strain measurement from a single sensor, on one face of the structure, and its analytical counterpart.

The SSB-iFEM and the standard iFEM are compared considering three thin-walled structures: a flat plate, a rectangular section box, and a C-section beam. Both numerical analyses and experimental tests are presented. The study reveals that the new SSB-iFEM

formulation demonstrates equivalent accuracy to the iFEM when back-to-back sensor configurations are adopted. Moreover, when considering sensors installed on one face only, the standard iFEM struggles to effectively reconstruct the considered structures' deformed shape. On the contrary, for these sensor configurations, the SSB-iFEM shows consistent and accurate displacement reconstructions in every considered condition, thus making it a more flexible and reliable solution for variable sensor configurations.

In conclusion, the proposed SSB-iFEM is an equivalent strategy to the inverse Finite Element Method that, however, can strongly reduce the requirement of strain sensors and extend the field of application of the iFEM to thin-walled structures where the number of available sensors is small and their installation on both sides of the structure is impractical. It is worth noting that, when employing sensor configurations that do not consider back-to-back sensors, the SSB-iFEM reconstruction is successful only if built-up structures, such as the rectangular section box or the C-section beam, are considered: the deformed shape of the flat plate, with sensors placed only on one of its faces, would result impossible to reconstruct even for the SSB-iFEM as, with those input data, the accuracy of the reconstruction would sharply decrease. Nonetheless, this result is not concerning, as the objective of the SSB-iFEM is not to comprehend every possible sensor configuration that can be installed on a structure, but rather to expand the search space of possible sensor configurations when monitoring that structure.

In this regard, the study of the SSB-iFEM formulation should continue by comprehensively addressing the method's sensitivity to different sensor configurations, investigating optimization analysis to obtain optimal sensor patterns and strain expansion strategies to further reduce the number of required sensors, so to develop an efficient shape sensing procedure. In future works, the experimental validation of the formulation should also be considered.

CRediT authorship contribution statement

Vincenzo Biscotti: Writing – original draft, Visualization, Validation, Software, Formal analysis, Conceptualization. **Marco Esposito:** Writing – review & editing, Writing – original draft, Supervision, Methodology, Investigation, Formal analysis, Conceptualization. **Marco Gherlone:** Writing – review & editing, Supervision, Resources, Project administration, Conceptualization.

Declaration of competing interest

The authors declare the following financial interests/personal relationships which may be considered as potential competing interests: Vincenzo Biscotti reports financial support was provided by Italian Ministry of University and Research (MUR). If there are other authors, they declare that they have no known competing financial interests or personal relationships that could have appeared to influence the work reported in this paper.

Acknowledgments

Vincenzo Biscotti and Marco Gherlone acknowledge the support of the Italian Ministry of University and Research (MUR) and the Sustainable Mobility Center (MOST) through the project PNRR - M4C2 - CNMS - Spoke 1, funded under the scheme CN00000023 - PNRR – M4C2 Inv. 1.4 with grant agreement num. 55_PRR22_1155_22_GG002138

Appendix. In-depth comparison between the iFEM and the SSB-iFEM formulation

The results presented in Section 3.2.2, 3.3.4, and 3.4.4 highlight that, when back-to-back strain measurements are provided as input data for the analysis, the iFEM and the SSB-iFEM formulation produce equivalent and yet non-identical results. To investigate the factors that influence this outcome, the equations of the coefficient matrix and the constant term of the SSB-iFEM formulation (Eqs. (27) and (28)) have to be rewritten in order to explicit the same terms contained in the expressions of the coefficient matrix and the constant term of the iFEM (Eqs. (15) and (16)), so to obtain an equivalent expression. Before even beginning to work on the equations, it can be immediately observed that, for both the coefficient matrix and the constant term, the two formulations share the terms related to the transverse shear strains. Therefore, in order to compare the two formulations, only the terms of the SSB-iFEM formulation related to the in-plane strain measurements have to be rewritten. Furthermore, observing the expressions of Eqs. (27) and (28), it is evident that the terms related to the top and bottom measurements have an identical formulation. As a consequence, the objective becomes simply to rewrite these expressions:

$$(\mathbf{K}_p)^e = \frac{1}{A^e}\int_{A^e}\left[(\mathbf{B}^{mk})^T(\mathbf{Z}_{\varepsilon_p}(z))^T diag(\lambda_p)\mathbf{Z}_{\varepsilon_p}(z)\mathbf{B}^{mk}\right] dA^e \tag{A.1}$$

$$(\mathbf{f}_p)^e = \frac{1}{A^e}\int_{A^e}\left[(\mathbf{B}^{mk})^T(\mathbf{Z}_{\varepsilon_p}(z))^T diag(\lambda_p)\boldsymbol{\varepsilon}_p\right] dA^e \tag{A.2}$$

where the dependence of the vector of penalization factors, $\boldsymbol{\lambda}_p$, and of the in-plane strain measurements, $\boldsymbol{\varepsilon}_p$, from the z coordinate is omitted and where a generic value of z is considered for the expression of $\mathbf{Z}_{\varepsilon_p}$.

The first step to rewrite Eqs. (A.1) and (A.2) is to explicit the terms $\mathbf{B}^{mk}$, $\mathbf{Z}_{\varepsilon_p}(z)$ and $\boldsymbol{\varepsilon}_p$, which were presented respectively in Eq. (20), (18), and (4).

After introducing all the proper explicit expressions, Eqs. (A.1) and (A.2) are rewritten as:

$$(\mathbf{K}_p)^e = \frac{1}{A^e}\int_{A^e}\begin{bmatrix}(\mathbf{B}^m)^T & (\mathbf{B}^k)^T\end{bmatrix}\begin{bmatrix}\mathbf{I}^T\\ z\mathbf{I}^T\end{bmatrix} diag(\lambda_p)\begin{bmatrix}\mathbf{I} & z\mathbf{I}^T\end{bmatrix}\begin{bmatrix}\mathbf{B}^m\\ \mathbf{B}^k\end{bmatrix} dA^e \tag{A.3}$$

$$(\mathbf{f}_p)^e = \frac{1}{A^e}\int_{A^e}\begin{bmatrix}(\mathbf{B}^m)^T & (\mathbf{B}^k)^T\end{bmatrix}\begin{bmatrix}\mathbf{I}^T\\ z\mathbf{I}^T\end{bmatrix} diag(\lambda_p)(\mathbf{m}^\epsilon + z\mathbf{k}^\epsilon)\, dA^e \tag{A.4}$$

Computing the matrix and vector products of Eqs. (A.3) and (A.4), the following expressions are obtained:

$$(\mathbf{K}_p)^e = \frac{1}{A^e}\int_{A^e}\begin{pmatrix}(\mathbf{B}^m)^T diag(\lambda_p)\mathbf{B}^m + \\ +2z(\mathbf{B}^m)^T diag(\lambda_p)\mathbf{B}^k + \\ +z^2(\mathbf{B}^k)^T diag(\lambda_p)\mathbf{B}^k\end{pmatrix} dA^e \tag{A.5}$$

$$(\mathbf{f}_p)^e = \frac{1}{A^e}\int_{A^e}\begin{pmatrix}(\mathbf{B}^m)^T diag(\lambda_p)\mathbf{m}^\epsilon + \\ +z(\mathbf{B}^m)^T diag(\lambda_p)\mathbf{k}^\epsilon + \\ +z(\mathbf{B}^k)^T diag(\lambda_p)\mathbf{m}^\epsilon + \\ +z^2(\mathbf{B}^k)^T diag(\lambda_p)\mathbf{k}^\epsilon\end{pmatrix} dA^e \tag{A.6}$$

where now the terms $\mathbf{B}^m$, $\mathbf{B}^k$, $\mathbf{m}^\epsilon$, and $\mathbf{k}^\epsilon$ of the iFEM formulation appear explicitly. The expressions of Eqs. (A.5) and (A.6) are to be specialized for the top and bottom surface in order to compute the equivalent expression of the coefficient matrix and the constant term of the SSB-iFEM formulation. Moreover, as mentioned previously, the equivalence between the two formulations requires back-to-back sensor configurations as input for the analysis. Assuming for simplicity the case where back-to-back strain rosettes are employed for all the elements (this choice is non-restrictive), the vector of penalization factors specialized for the top and the bottom surface of each element, λ_p^+ and λ_p^-, are identical and equal to unit vectors. Therefore, the terms of the coefficient matrix, $(\mathbf{K}_p^+)^e$ and $(\mathbf{K}_p^-)^e$, as well as the ones of the constant term, $(\mathbf{f}_p^+)^e$ and $(\mathbf{f}_p^-)^e$, can be simply obtained from Eqs. (A.5) and (A.6) by simplifying the diagonal matrix terms and setting $z = +t$ for the terms of the top surface and $z = -t$ for the terms of the bottom surface. Thus, adding each contribution as shown in Eqs. (26), the equivalent expressions for the coefficient matrix and the constant term of the SSB-iFEM formulation are obtained:

$$(\mathbf{K}')^e = \frac{1}{A^e}\int_{A^e}\begin{pmatrix}(\mathbf{B}^m)^T\mathbf{B}^m + \\ +t^2(\mathbf{B}^k)^T\mathbf{B}^k + \\ +\frac{1}{2}(\mathbf{B}^s)^T diag(\lambda_g)\mathbf{B}^s\end{pmatrix} dA^e \tag{A.7}$$

$$(\mathbf{f}')^e = \frac{1}{A^e}\int_{A^e}\begin{pmatrix}(\mathbf{B}^m)^T\mathbf{m}^\epsilon + \\ +t^2(\mathbf{B}^k)^T\mathbf{k}^\epsilon\end{pmatrix} dA^e \tag{A.8}$$

where, considering that the nodal displacements are computed as $(\mathbf{K}')^e\mathbf{u}^e = (\mathbf{f}')^e$, both terms were simplified by multiplying them by factor of $1/2$.

Eqs. (A.7) and (A.8) can be now compared to the original iFEM expressions of Eqs. (15) and (16). However, it is convenient to first rewrite the latter, to obtain the following expressions:

$$\mathbf{K}^e = \frac{1}{A^e}\int_{A^e}\begin{pmatrix}\zeta(\mathbf{B}^m)^T\mathbf{B}^m + \\ +(\omega t)^2(\mathbf{B}^k)^T\mathbf{B}^k + \\ +\xi(\mathbf{B}^s)^T diag(\lambda_g)\mathbf{B}^s\end{pmatrix} dA^e \tag{A.9}$$

$$\mathbf{f}^e = \frac{1}{A^e}\int_{A^e}\begin{pmatrix}\zeta(\mathbf{B}^m)^T\mathbf{m}^\epsilon + \\ +(\omega t)^2(\mathbf{B}^k)^T\mathbf{k}^\epsilon\end{pmatrix} dA^e \tag{A.10}$$

where each individual contribution of Eqs. (15) and (16) is added together to produce the iFEM coefficient matrix and constant term, and where the factors ζ, ω and ξ are introduced to facilitate the comparison between the two formulations. In the original iFEM formulation, $\zeta = 1$, $\omega = 2$, and $\xi = 1$.

Immediately, the term-to-term comparison of Eqs. (A.7) and (A.9), and of (A.8) and (A.10) highlights that to obtain a unique and identical formulation, the three factors would have to be set so that $\zeta = 1$, $\omega = 1$ and $\xi = 1/2$. Thus, this comparison demonstrates why the iFEM and the SSB-iFEM produce, in the case of back-to-back configurations, results that are slightly different from one another: the "weight" of the contributions to the elements coefficient matrices and constant terms, ζ, ω and ξ, are different between the two formulations. In particular, the dimensional coefficient $(2t)^2$ of the iFEM formulation appears to emphasize the contribution of the bending terms more than the equivalent term, t^2, of the SSB-iFEM formulation.

Data availability

Data will be made available on request.

References

[1] C.R. Farrar, K. Worden, An introduction to structural health monitoring, Philos. Trans. R. Soc. A: Math. Phys. Eng. Sci. 365 (1851) (2007) 303–315, http://dx.doi.org/10.1098/rsta.2006.1928.

[2] M. Gherlone, P. Cerracchio, M. Mattone, Shape sensing methods: Review and experimental comparison on a wing-shaped plate, Prog. Aerosp. Sci. 99 (2018) 14–26, http://dx.doi.org/10.1016/j.paerosci.2018.04.001.

[3] M. Li, D. Jia, Z. Wu, S. Qiu, W. He, Structural damage identification using strain mode differences by the iFEM based on the Convolutional Neural Network (CNN), Mech. Syst. Signal Process. 165 (2022) 108289, http://dx.doi.org/10.1016/j.ymssp.2021.108289.

[4] F. Ganjdoust, A. Kefal, A. Tessler, Delamination detection and localization in vibrating composite plates and shells using the inverse finite element method, Sensors 23 (18) (2023) http://dx.doi.org/10.3390/s23187926.

[5] R. Evenblij, F. Kong, C. Koimtzoglou, M. Ciminello, I. Dimino, A. Concilio, Shape sensing for morphing structures using fiber bragg grating technology, in: P.C. Wolcken, M. Papadopoulos (Eds.), Smart Intelligent Aircraft Structures, SARISTU, Springer International Publishing, Cham, 2016, pp. 471–491, http://dx.doi.org/10.1007/978-3-319-22413-8_21.

[6] G.C. Foss, E.D. Haugse, Using modal test results to develop strain to displacement transformations, in: Proceedings of the 13th International Conference on Modal Analysis, Nashville, 1995, https://api.semanticscholar.org/CorpusID:117880458.

[7] A. Pisoni, C. Santolini, D. Hauf, S. Dubowsky, Displacements in a vibrating body by strain gauge measurements, Proc. SPIE 2460 (2001) https://www.researchgate.net/publication/2460854_Displacements_In_A_Vibrating_Body_By_Strain_Gauge_Measurements.

[8] P. Bogert, E. Haugse, R. Gehrki, Structural shape identification from experimental strains using a modal transformation technique, in: 44th AIAA/ASME/ASCE/AHS/ASC Structures, Structural Dynamics, and Materials Conference, Norfolk, 2003, http://dx.doi.org/10.2514/6.2003-1626.

[9] S. Rapp, L.-H. Kang, J.-H. Han, U.C. Mueller, H. Baier, Displacement field estimation for a two-dimensional structure using fiber bragg grating sensors, Smart Mater. Struct. 18 (2) (2009) 025006, http://dx.doi.org/10.1088/0964-1726/18/2/025006.

[10] M. Freydin, M.K. Rattner, D.E. Raveh, I. Kressel, R. Davidi, M. Tur, Fiber-optics-based aeroelastic shape sensing, AIAA J. 57 (12) (2019) 5094–5103, http://dx.doi.org/10.2514/1.J057944.

[11] W.L. Ko, W.L. Richards, V.T. Fleischer, Displacement Theories for In-Flight Deformed Shape Predictions of Aerospace Structures, NASA/TP-2007-214612, Report NASA Dryden Flight Research Center, Edwards, CA, United States, 2007, https://ntrs.nasa.gov/citations/20070032936.

[12] W. Ko, W.L. Richards, V. Fleischer, Applications of ko displacement theory to the deformed shape predictions of the doubly-tapered ikhana wing, 2009, NASA/ TP- 2009- 214652, https://ntrs.nasa.gov/citations/20090040594.

[13] C.V. Jutte, W.L. Ko, C.A. Stephens, J.A. Bakalyar, W.L. Richards, Deformed shape calculation of a full-scale wing using fiber optic strain data from a ground loads test, 2011, NASA/ TP- 2011- 215975, https://ntrs.nasa.gov/citations/20120004140.

[14] C. Pak, Wing shape sensing from measured strain, AIAA J. 54 (3) (2016) 1068–1077, http://dx.doi.org/10.2514/1.J053986.

[15] S.Z. Guoping Ding, W. Song, Strain - deformation reconstruction of CFRP laminates based on Ko displacement theory, Nondestruct. Test. Eval. 36 (2) (2021) 145–157, http://dx.doi.org/10.1080/10589759.2019.1707200.

[16] A. Tessler, J. Spangler, A least-squares variational method for full-field reconstruction of elastic deformations in shear-deformable plates and shells, Comput. Methods Appl. Mech. Engrg. 194 (2) (2005) 327–339, http://dx.doi.org/10.1016/j.cma.2004.03.015, Selected papers from the 11th Conference on The Mathematics of Finite Elements and Applications.

[17] A. Kefal, E. Oterkus, A. Tessler, J.L. Spangler, A quadrilateral inverse-shell element with drilling degrees of freedom for shape sensing and structural health monitoring, Eng. Sci. Technol. Int. J. 19 (3) (2016) 1299–1313, http://dx.doi.org/10.1016/j.jestch.2016.03.006.

[18] A. Kefal, An efficient curved inverse-shell element for shape sensing and structural health monitoring of cylindrical marine structures, Ocean Eng. 188 (2019) 106262, http://dx.doi.org/10.1016/j.oceaneng.2019.106262.

[19] A. Kefal, E. Oterkus, Isogeometric iFEM analysis of thin shell structures, Sensors 20 (9) (2020) http://dx.doi.org/10.3390/s20092685.

[20] E. Del Priore, L. Lampani, A methodology for applying isogeometric inverse finite element method to the shape sensing of stiffened thin-shell structures, Thin-Walled Struct. 199 (2024) 111837, http://dx.doi.org/10.1016/j.tws.2024.111837.

[21] A. Tessler, R. Roy, M. Esposito, C. Surace, M. Gherlone, Shape sensing of plate and shell structures undergoing large displacements using the inverse finite element method, Shock. Vib. 2018 (1) (2018) 8076085, http://dx.doi.org/10.1155/2018/8076085.

[22] M. Li, D. Jia, H. Huang, Geometrically nonlinear deformation reconstruction based on iqs4 elements using a linearized iterative iFEM algorithm, Acta Mech. Solida Sin. 36 (2023) 166–180, http://dx.doi.org/10.1007/s10338-022-00369-6.

[23] P. Cerracchio, M. Gherlone, M. Di Sciuva, A. Tessler, A novel approach for displacement and stress monitoring of sandwich structures based on the inverse finite element method, Compos. Struct. 127 (2015) 69–76, http://dx.doi.org/10.1016/j.compstruct.2015.02.081.

[24] A. Kefal, A. Tessler, E. Oterkus, An enhanced inverse finite element method for displacement and stress monitoring of multilayered composite and sandwich structures, Compos. Struct. 179 (2017) 514–540, http://dx.doi.org/10.1016/j.compstruct.2017.07.078.

[25] F. Zhao, H. Bao, J. Liu, K. Li, Shape sensing of multilayered composite and sandwich beams based on refined zigzag theory and inverse finite element method, Compos. Struct. 261 (2021) 113321, http://dx.doi.org/10.1016/j.compstruct.2020.113321.

[26] M. Gherlone, P. Cerracchio, M. Mattone, M. Di Sciuva, A. Tessler, Shape sensing of 3D frame structures using an inverse finite element method, Int. J. Solids Struct. 49 (22) (2012) 3100–3112, http://dx.doi.org/10.1016/j.ijsolstr.2012.06.009.

[27] F. Zhao, L. Xu, H. Bao, J. Du, Shape sensing of variable cross-section beam using the inverse finite element method and isogeometric analysis, Measurement 158 (2020) 107656, http://dx.doi.org/10.1016/j.measurement.2020.107656.

[28] R. Roy, M. Gherlone, C. Surace, A shape sensing methodology for beams with generic cross-sections: Application to airfoil beams, Aerosp. Sci. Technol. 110 (2021) 106484, http://dx.doi.org/10.1016/j.ast.2020.106484.

[29] M. Esposito, R. Roy, C. Surace, M. Gherlone, Hybrid shell-beam inverse finite element method for the shape sensing of stiffened thin-walled structures: Formulation and experimental validation on a composite wing-shaped panel, Sensors 23 (13) (2023) http://dx.doi.org/10.3390/s23135962.

[30] E.J. Miller, R. Manalo, A. Tessler, Full-field reconstruction of structural deformations and loads from measured strain data on a wing using the inverse finite element method, 2016, NASA/ TM- 2016- 219407, https://ntrs.nasa.gov/citations/20160014695.

[31] U. Papa, S. Russo, A. Lamboglia, G.D. Core, G. Iannuzzo, Health structure monitoring for the design of an innovative UAS fixed wing through inverse finite element method (iFEM), Aerosp. Sci. Technol. 69 (2017) 439–448, http://dx.doi.org/10.1016/j.ast.2017.07.005.

[32] D. Oboe, L. Colombo, C. Sbarufatti, M. Giglio, Shape sensing of a complex aeronautical structure with inverse finite element method, Sensors 21 (4) (2021) http://dx.doi.org/10.3390/s21041388.

[33] F. Valoriani, M. Esposito, M. Gherlone, Shape sensing for an UAV composite half-wing: Numerical comparison between modal method and Ko's displacement theory, Aerospace 9 (9) (2022) https://www.mdpi.com/2226-4310/9/9/509.

[34] A. Kefal, E. Oterkus, Displacement and stress monitoring of a panamax containership using inverse finite element method, Ocean Eng. 119 (2016) 16–29, http://dx.doi.org/10.1016/j.oceaneng.2016.04.025.

[35] A. Kefal, E. Oterkus, Displacement and stress monitoring of a chemical tanker based on inverse finite element method, Ocean Eng. 112 (2016) 33–46, http://dx.doi.org/10.1016/j.oceaneng.2015.11.032.

[36] J. Wang, L. Ren, R. You, T. Jiang, Z. Jia, G. xin Wang, Experimental study of pipeline deformation monitoring using the inverse finite element method based on the iBeam3 element, Measurement 184 (2021) 109881, http://dx.doi.org/10.1016/j.measurement.2021.109881.

[37] P. Savino, F. Tondolo, Two-node curved inverse finite element formulations based on exact strain-displacement solution, J. Appl. Comput. Mech. 9 (1) (2023) 259–273, http://dx.doi.org/10.22055/jacm.2022.41150.3708.

[38] R. Roy, M. Gherlone, C. Surace, A. Tessler, Full-field strain reconstruction using uniaxial strain measurements: Application to damage detection, Appl. Sci. 11 (4) (2021) http://dx.doi.org/10.3390/app11041681.

[39] A. Kefal, C. Diyaroglu, M. Yildiz, E. Oterkus, Coupling of peridynamics and inverse finite element method for shape sensing and crack propagation monitoring of plate structures, Comput. Methods Appl. Mech. Engrg. 391 (2022) 114520, http://dx.doi.org/10.1016/j.cma.2021.114520.

[40] F. Ganjdoust, A. Kefal, A. Tessler, A novel delamination damage detection strategy based on inverse finite element method for structural health monitoring of composite structures, Mech. Syst. Signal Process. 192 (2023) 110202, http://dx.doi.org/10.1016/j.ymssp.2023.110202.
[41] R. Roy, M. Gherlone, Delamination and skin-spar debond detection in composite structures using the inverse finite element method, Materials 16 (5) (2023) http://dx.doi.org/10.3390/ma16051969.
[42] M. Esposito, M. Gherlone, Composite wing box deformed-shape reconstruction based on measured strains: Optimization and comparison of existing approaches, Aerosp. Sci. Technol. 99 (2020) 105758, http://dx.doi.org/10.1016/j.ast.2020.105758.
[43] M. Esposito, M. Gherlone, Material and strain sensing uncertainties quantification for the shape sensing of a composite wing box, Mech. Syst. Signal Process. 160 (2021) 107875, http://dx.doi.org/10.1016/j.ymssp.2021.107875.
[44] A. Tessler, J.L. Spangler, M. Gherlone, M. Mattone, M. Di Sciuva, Real-time characterization of aerospace structures using onboard strain measurement technologies and inverse finite element method, Struct. Heal. Monitoring- an Int. J. 1 (2011) 981–988, https://api.semanticscholar.org/CorpusID:56118098.
[45] Z. Zhao, K. Chen, Y. Liu, H. Bao, A large-scale sensor layout optimization algorithm for improving the accuracy of inverse finite element method, Sensors 23 (19) (2023) http://dx.doi.org/10.3390/s23198176.
[46] A. Tessler, H. Riggs, C.E. Freese, G.M. Cook, An improved variational method for finite element stress recovery and a posteriori error estimation, Comput. Methods Appl. Mech. Engrg. 155 (1) (1998) 15–30, http://dx.doi.org/10.1016/S0045-7825(97)00135-7.
[47] A. Kefal, I.E. Tabrizi, M. Yildiz, A. Tessler, A smoothed iFEM approach for efficient shape-sensing applications: Numerical and experimental validation on composite structures, Mech. Syst. Signal Process. 152 (2021) 107486, http://dx.doi.org/10.1016/j.ymssp.2020.107486.
[48] D. Oboe, L. Colombo, C. Sbarufatti, M. Giglio, Comparison of strain pre-extrapolation techniques for shape and strain sensing by iFEM of a composite plate subjected to compression buckling, Compos. Struct. 262 (2021) 113587, http://dx.doi.org/10.1016/j.compstruct.2021.113587.
[49] R. Roy, A. Tessler, C. Surace, M. Gherlone, Efficient shape sensing of plate structures using the inverse finite element method aided by strain pre-extrapolation, Thin-Walled Struct. 180 (2022) 109798, http://dx.doi.org/10.1016/j.tws.2022.109798.
[50] R. Roy, M. Esposito, C. Surace, M. Gherlone, A. Tessler, Shape sensing of stiffened plates using inverse FEM aided by virtual strain measurements, in: P. Rizzo, A. Milazzo (Eds.), European Workshop on Structural Health Monitoring, Springer International Publishing, Cham, 2023, pp. 454–463, http://dx.doi.org/10.1007/978-3-031-07254-3_46.
[51] K. Grattan, T. Sun, Fiber optic sensor technology: an overview, Sensors Actuators A: Phys. 82 (1) (2000) 40–61, http://dx.doi.org/10.1016/S0924-4247(99)00368-4.